THESIS

DEMONSTRATION OF FILAMENT-GUIDED ELECTRICAL DISCHARGES FROM A HIGH AVERAGE POWER 1 KHZ PICOSECOND LASER

Submitted by

Kristian A. Dehne

Department of Electrical and Computer Engineering

In partial fulfillment of the requirements

For the Degree of Master of Science

Colorado State University

Fort Collins, Colorado

Spring 2023

Master's Committee:

Advisor: Jorge Rocca

Mario Marconi
Samuel Brewer

ABSTRACT

DEMONSTRATION OF FILAMENT-GUIDED ELECTRICAL DISCHARGES FROM A HIGH AVERAGE POWER 1 KHZ PICOSECOND LASER

The atmospheric propagation of ultrashort, high energy laser pulses is of interest for applications including remote sensing, directed energy, and the guiding of lightning. In this thesis, the filamentation of high energy picosecond laser pulses at repetition rates up to 1 kHz is demonstrated and the guiding of electrical discharges in air at high repetition rates is studied. The design and performance of the diode-pumped Yb:YAG chirped pulse amplification (CPA) system utilized for this experiment is also described.

Diode-pumped solid state lasers in a CPA layout have emerged as the modern choice for the generation of high pulse energies at high repetition rates. For the work presented in this thesis, a high average power diode-pumped Yb:YAG laser system utilized for filament formation is detailed. The compact CPA system, which combines a room temperature regenerative amplifier and cryogenically cooled Yb:YAG amplifiers, results in compressed pulses of < 5 ps duration with up to 1.1 J of energy at 1 kHz repetition rate. This record Joule-level 1 kHz repetition rate picosecond laser (average power output of more than 1 kW) has enabled the results described herein.

The application of this high average power Yb:YAG system for producing laser guided electrical discharges is the main focus of this thesis. The compressed output pulses from the Yb:YAG laser induce filamentation in air, resulting from the counterbalance between Kerr self-focusing and plasma refraction defocusing. The hydrodynamic response of the atmospheric air results in a density depression of similar geometry to the filament. The result is a preferential path which both triggers and guides electrical discharges. The majority of previous laser-guided discharge studies have been conducted at repetition rates of 10 Hz, where the medium completely recovers before the next laser pulse arrives. This thesis reports on the physics of laser filament-guided electric

discharges in air initiated by high energy (up to 250 mJ) 1030 nm wavelength laser pulses of $\sim$7 ps duration at repetition rates up to 1 kHz. A breakdown voltage reduction of up to 4.2 X was measured and determined to result primarily from the perturbation caused by a single laser pulse, with cumulative effects playing only a secondary role. A current proportional to the laser pulse energy arises as soon as the laser pulse arrives, initiating a high impedance phase of the discharge channel evolution. Full breakdown, characterized by impedance collapse and the onset of high current conduction, occurs 100s of ns to a few μs later. The gaps between the filamentary plasma channel and the electrodes are observed to play a role in the delay between arrival of the laser pulse and the onset of a discharge. The breakdown voltages measured for 100 Hz and 1 kHz repetition rates are shown to be nearly equivalent. This is consistent with the results of interferometric analysis which shows that the filament formed by a single laser shot causes a deep density depression up to 75%, compared with the 20% density depression measured 10 μs prior to the arrival of a laser pulse in a sustained 1 kHz sequence. The physical insight gained from this work on the formation of laser filament-guided discharges in air at 1 kHz repetition rate can be expected to contribute to their use in applications.

ACKNOWLEDGEMENTS

I would like to thank my advisor, Professor Jorge Rocca. I am grateful for the opportunities and guidance that Dr. Rocca has given me to develop skills and experience in laser research and engineering.

I owe a special thanks to my colleagues in the diode-pumped laser lab of the Advanced Beam Laboratory: Brendan Reagan, Cory Baumgarten, Han Chi, and Yong Wang. I have learned a tremendous amount from each of them and I have enjoyed working alongside them.

I would also like to thank all of the people that I have worked with over the years in the ABL and ERC including Alex Meadows, Gabe Murray, Hugh Currah, Byron Fritch, Adam Higginson, Hanchen Wang, Liang Yin, Reed Hollinger, Herman Bravo, Aaron Davenport, Shoujun Wang, Vladimir Chvykov, Emmett Randel, Ryan Nedbailo, Sergio Oloriz, Elzbieta Jankowska, and many others. I am very fortunate to work with such intelligent and dedicated people.

Most importantly, I'm thankful to my family and friends for their constant support, which has enabled me to achieve my goals.

DEDICATION

I dedicate this thesis to my family and friends.

TABLE OF CONTENTS

ABSTRACT ii
ACKNOWLEDGEMENTS iv
DEDICATION v

Chapter 1 Introduction 1
1.1 Progress in Ultrafast Laser Development 1
1.1.1 Mode Locking 2
1.1.2 Chirped Pulse Amplification 5
1.2 Scaling Ultrafast Lasers to High Average Power 9
1.2.1 Diode Pumped Solid State Lasers 10
1.2.2 Rare Earth Ion-Doped Materials 11
1.2.3 Yb:YAG at Cryogenic Temperature 14
1.2.4 Current Status of High Average Power, High Pulse Energy, Diode-Pumped Lasers 18
1.2.5 Applications 20
1.3 High Power Laser Propagation in Air: Filamentation 21
1.3.1 Filament-Guided Electrical Discharges in Air 23
1.4 Outline of Thesis Content 25

Chapter 2 kW-Class Diode Pumped Yb:YAG Laser 26
2.1 Introduction and System Overview 26
2.2 Passively Mode Locked Oscillator 28
2.3 Pulse Stretcher 31
2.4 Regenerative Preamplifier 33
2.5 Power Amplifiers and System Performance 36
2.5.1 Yb:YAG Crystal 36
2.5.2 2nd Stage Amplifier 37
2.5.3 3rd Stage Amplifier 39
2.6 Pulse Compressor 41
2.7 Summary and Applications 44

Chapter 3 Picosecond Laser Filament Guiding of Electrical Discharges in Air at 1 kHz Repetition Rate 45
3.1 Introduction 45
3.2 Experimental Setup and Methodology 49
3.3 Results and Discussion 52
3.3.1 Discharges at 1 kHz 52
3.3.2 Breakdown voltage thresholds 53
3.3.3 Discharge delay time 55
3.3.4 Breakdown voltage reduction 56
3.3.5 Initial current flow and breakdown 60

3.3.6 Streamerless discharge formation 63
3.4 Conclusions 65

Chapter 4 Summary 67

Bibliography 70

Chapter 1

Introduction

1.1 Progress in Ultrafast Laser Development

Following the demonstration of the first laser in 1960 [1], a decade of rapid development solidified the role of lasers as invaluable tools for scientific research, and later for defense and industry. Driven by the potential applications for this technology, progress continues to be made in advancing laser performance capabilities. It is shown below in Figure 1.1 that the development of powerful ultrafast lasers, with pulse durations below 100 picoseconds (1 ps = 10^{-12} s), reaching femtoseconds (1 fs = 10^{-15} s), was the culmination of decades of work to produce shorter and more intense laser pulses.

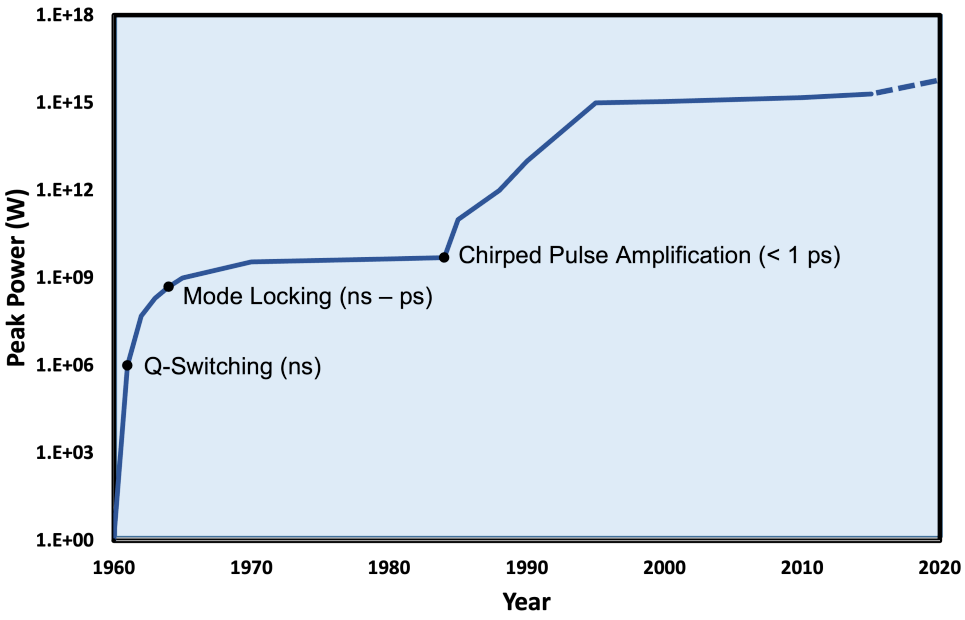

Figure 1.1: Advancements in laser peak power and pulse duration since 1960.

Shortly after Maiman's ruby laser, a method for producing powerful short pulses was created, called Q-switching [2]. This is achieved by building a cavity around the gain medium and intro-

ducing high loss to this cavity, via an attenuator, to prevent lasing from occurring. The absence of feedback allows more energy to be stored in the gain medium as pumping continues. At the point of saturation, a population inversion many times greater than the threshold for lasing is attained. The cavity loss is then rapidly decreased, leading to strong amplification and the formation of a short and very intense laser pulse. The invention of Q-switching was an important step towards shorter pulse durations and the technique is still commonly used today. However, the minimum pulse durations achievable from Q-switching are still in the nanosecond range. The real shift into ultrashort durations in the picosecond to femtosecond range came from the development of mode-locking, which was first demonstrated in 1964 [3, 4].

1.1.1 Mode Locking

The development of mode locking paved the way for sub-picosecond pulse durations. In mode locked lasers, one of several techniques is employed to achieve ultrashort pulse durations from an oscillator [5]. Within a laser cavity, a number of longitudinal modes will oscillate if the gain bandwidth of the material, $\Delta\nu$, is larger than the mode spacing within the cavity. The frequency separation between each mode is related to the round trip time in the resonator, t_r:

$$\frac{1}{t_r} = \frac{c}{2n_0 L} \tag{1.1}$$

where c is the speed of light, n_0 is the index of refraction for the medium, and $2L$ is the round-trip length of the cavity (for the case in which the gain medium extends the length of the cavity). These modes oscillate independently of one another in the cavity and exhibit a random distribution of phases. In the absence of mode locking, the laser output will have a total electric field which is a superposition of the various modes. This can be expressed by [6, 7]:

$$E(t) = \sum_{n=-m}^{m} A_n e^{i(2\pi\nu_n t + \varphi_n)} \tag{1.2}$$

where, for the nth mode, A_n is the amplitude and φ_n is the phase. The frequency is given by $\nu_n = \nu_0 + n\Delta\nu$ where ν_0 is the central mode frequency, n is the index of refraction, and $\Delta\nu$ is the frequency bandwidth. In this case where the amplitude and phase of each mode are random, the laser intensity is given by:

$$I = K\left|E\left(t\right)\right|^2 = K\left|\sum_{n=-m}^{m} A_n e^{i(2\pi n\Delta\nu t+\varphi_n)}\right|^2 \tag{1.3}$$

$$= K\sum_{n}\left|A_n\right|^2 + K\sum_{n\neq m}\sum_{m} A_n A_m^* e^{i[2\pi(n-m)\Delta\nu t+(\varphi_n-\varphi_m)]} \tag{1.4}$$

with constant of proportionality, K. With a random distribution of phases for a large number of oscillating modes, the second term in equation (1.4) above becomes very small. As a result, the output intensity is equal to the first term which is a sum of the fluctuating mode intensities.

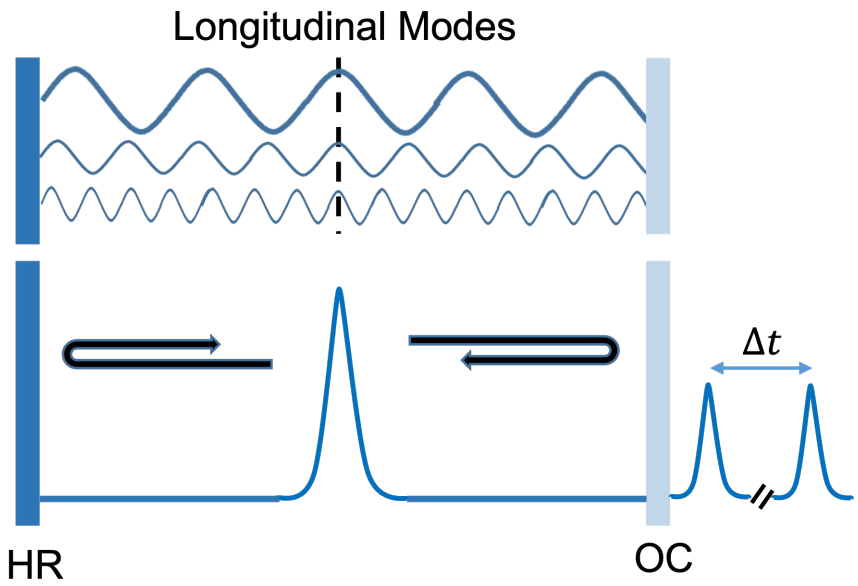

Figure 1.2: Illustration of the mode locking process: longitudinal modes constructively interfere producing an ultrafast pulse which oscillates between a high reflector (HR) and an output coupler (OC) from which a train of ultrafast pulses separated by Δt are emitted.

The goal of mode locking is to achieve a fixed phase relationship between these oscillating modes, as shown in Figure 1.2. In this scenario, the modes will periodically interfere constructively at an arbitrary time where the phase for each mode is equal. If the amplitude of each mode is also assumed to be equal, the laser output intensity can be expressed as:

$$I = I_0 \left| \sum_{n=-m}^{m} e^{2\pi i \nu_n t} \right|^2 \tag{1.5}$$

with $I_0 = KA_0^2$. In which case, the variation of the output intensity with time can be expressed as:

$$I = I_0 \left[\frac{\sin\left[\pi\left(N+1\right)\Delta\nu \mathrm{t}\right]}{\sin\left(\pi \Delta\nu t\right)} \right]^2 \tag{1.6}$$

which gives a series of pulses separated in time, Δt, by the round-trip time of the cavity, t_r (see Fig. 1.2). As the pulse oscillates within the cavity, a portion is transmitted each round trip with peak intensity:

$$I_{peak} \approx N^2 I_0 \tag{1.7}$$

taken as the limit of the argument of the sine function in the denominator of equation (1.6) approaches zero. Compared with a non mode-locked laser, the intensity of a mode-locked pulse is increased by a factor equivalent to the number of oscillating modes. This is true for the unrealistic case where all modes within the gain bandwidth are locked together. The transform limited pulse duration for a mode-locked oscillator also factors in the pulse shape. For a given mode-locked bandwidth, $N\Delta\nu$, the minimum pulse duration, t_p, is:

$$t_p = \frac{\alpha}{N\Delta\nu} \tag{1.8}$$

where α is the time-bandwidth product which depends on the pulse shape. For a Gaussian pulse shape this value is 0.441 and 0.315 for a $sech^2$ shape. From equation (1.8), it is apparent that the minimum pulse duration is inversely proportional to the number of modes. This makes

laser materials with a broad gain bandwidth ideal for achieving ultrashort pulse durations from mode-locked lasers.

In order to create the phase relationship described above, mode locking is typically categorized by use of "active" or "passive" methods [7]. For actively mode-locked lasers, an external signal is produced by an acousto-optic or electro-optic device to modulate the frequency or amplitude of the oscillating light, respectively. By synchronizing the rate of this modulation, the necessary phase relationship can be achieved for mode locking. The use of external signals to drive the modulation imposes limitations on the minimum pulse durations that can be achieved. This is where passively mode locked lasers have an advantage. In passive mode locking, apart from Kerr lens mode locking [8], an optical element is used that enables self-modulation of the amplitude depending on intensity. These elements, called saturable absorbers, introduce loss by absorption for low intensity light that decreases with increasing intensity. This has the effect of promoting amplification of higher intensity pulses which oscillate until mode locking occurs. By achieving mode-locking from the oscillating signals within the cavity, the use of a passive element allows for much shorter pulse durations.

Initially, mode locking enabled the generation of picosecond pulse durations. With further development, alongside other solutions emanating from laser research, such as dispersion compensation, mode-locked solid-state lasers with femtosecond pulses were available by the 1990s [9]. While this technique allows for ultrashort pulses at high repetition rates, the pulse energy is typically at the nanojoule level. At the time, this created a situation where the energy of the ultrafast pulses was limited due to the adverse effects of amplifying at such high intensity that optical elements and the gain medium itself could be damaged. In order to achieve ultrafast pulses with high peak power, further advancements were necessary.

1.1.2 Chirped Pulse Amplification

The breakthrough in developing high energy ultrafast lasers came with the invention of chirped pulse amplification (CPA) in 1985 by Strickland and Mourou [10]. The CPA technique employs a

system design which involves reducing the intensity of the pulses prior to amplification by stretching them in time, as shown in Figure 1.3. Following amplification, the pulses are re-compressed to their ultrashort duration. Prior to this development, master-oscillator power-amplifier (MOPA) systems could only attempt to manage pulse intensity by increasing beam size. As a result, pulses with extremely high peak power were possible, allowing new applications to be explored.

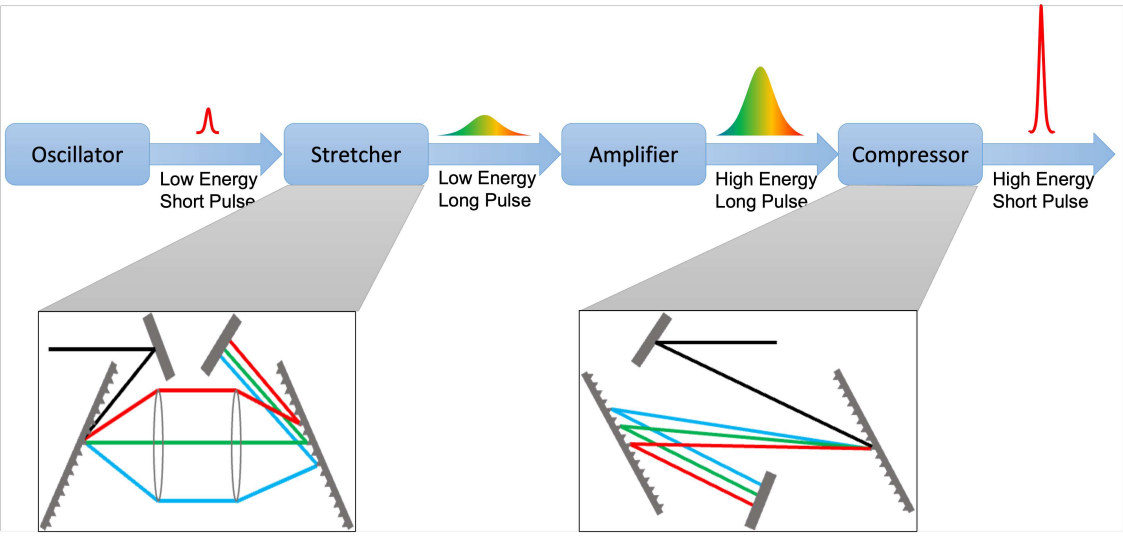

Figure 1.3: An illustration of a chirped pulse amplification (CPA) system layout. Low energy, short duration pulses are sent from an oscillator through a temporal stretcher which imparts positive dispersion. This results in low energy, long duration pulses which are safe to amplify to high energy. A compressor imparts negative dispersion to return the pulses to their original short duration, resulting in a final output of high energy, short pulses.

The CPA process typically starts with a mode-locked oscillator as the source of ultrashort, low energy pulses. As described in the previous section, these sources utilize broadband gain materials to generate ultrashort pulse durations at high repetition rates with low pulse energies. In order to reduce the intensity of the pulses, a stretcher is used to create a wavelength dependent time delay, or "chirp", in the pulse. Before the stretcher, the transform-limited oscillator pulses have zero spectral chirp, and all frequency components travel simultaneously. Dispersive elements impart chirp by altering the optical path difference between the high and low frequency components of the pulse. Various types of elements such as diffraction gratings, chirped mirrors, Bragg gratings, and optical fibers can be utilized in stretchers [11].

The effects of a dispersive medium on an optical pulse can be described by approximating the frequency dependent spectral phase $\varphi(\omega)$ with a Taylor series expansion about the central frequency ω_0 [12, 13]:

$$\varphi(\omega) = \sum_{n=0}^{\infty} \frac{\varphi^n(\omega_0)}{n!} * (\omega - \omega_0)^n \text{ with } \varphi^n(\omega_0) = \left.\frac{d^n \varphi(\omega)}{d\omega^n}\right|_{\omega_0} \tag{1.9}$$

$$\varphi(\omega) = \varphi(\omega_0) + \varphi'|_{\omega_0}(\omega - \omega_0) + \frac{1}{2}\varphi''|_{\omega_0}(\omega - \omega_0)^2 + \frac{1}{6}\varphi'''|_{\omega_0}(\omega - \omega_0)^3 + \ldots \tag{1.10}$$

In this expression, the zeroth-order coefficient $\varphi(\omega_0)$ is a constant phase called the carrier-envelope phase (CEP) which does not affect the intensity of light through the medium. The first order spectral phase term $\varphi'|_{\omega_0}$ describes the time domain translation called the group delay (GD). The group delay dispersion (GDD) is the second order phase term $\varphi''|_{\omega_0}$ at which the temporal structure of the electric field is altered. Beyond this, the third and fourth order dispersion terms create pre/post pulses and broaden the temporal shape, respectively.

Diffraction gratings are ideally suited for use in stretching and compressing pulses in most CPA systems [14, 15]. For a diffraction grating, the line density N (usually given in lines per mm) and the angles of the incident (θ_i) and diffracted (θ_d) beams are related by the grating equation:

$$\sin\theta_i + \sin\theta_d = m\lambda N \tag{1.11}$$

where λ is the wavelength of the incident light and m is the diffraction order. From the grating equation (1.11), it is shown that the diffracted angle depends on wavelength. By solving for the diffracted angle, θ_d, and taking the derivative with respect to the wavelength λ, the angular dispersion is expressed by:

$$\frac{d\theta_d}{d\lambda} = \frac{mN}{cos\theta_d} \tag{1.12}$$

The angular dispersion is then related to the temporal delay by the expression:

$$\frac{d\tau}{d\lambda} = \frac{d\tau}{d\theta_d}\frac{d\theta_d}{d\lambda} \;\; with \;\; \frac{d\tau}{d\theta_d} = \frac{1}{c}\frac{m\lambda DN}{cos^2\theta_d} \tag{1.13}$$

where $\frac{d\tau}{d\theta}$ is the rate of change of the group delay ($\tau = \frac{d\varphi}{d\omega}$) with diffracted angle θ_d and grating separation D. Finally, the group delay dispersion (GDD) for a grating pair can be found from the relation with the temporal dispersion [12, 13]:

$$\frac{d^2\varphi}{d\omega^2} = -\frac{D\lambda^2}{2\pi c}\frac{d\tau}{d\lambda} = -\frac{Dm^2\lambda^3N^2}{2\pi c^2 cos^3\theta_d} \tag{1.14}$$

When a short pulse propagates through common optical materials, a positive (normal) group delay dispersion occurs for the spectral components. In deriving the expression for second order dispersion, Treacy [14] showed that the group delay dispersion for a grating pair will always be negative (anomalous), independent of angle and separation. However, by adding a pair of lenses to image the first grating behind the second, Martinez created a method which effectively creates a negative distance between the gratings, allowing for positive dispersion [15]. Though the first CPA laser utilized a stretcher based on dispersion in an optical fiber producing anomalous dispersion, practically all modern systems use stretchers based on diffraction gratings that create positive dispersion and compressors that compensate with negative dispersion.

Upon entering the stretcher, the positive dispersion causes the high-frequency components of the pulse to trail the low-frequency components. A mirror after the second grating sends the beam back along the same path (see left inset in Fig. 1.3), necessitating a factor of 2 in equation (1.14), where the spectral components are recombined before exiting the stretcher. The result of this positive chirp is an increase in pulse duration by several orders of magnitude, and a corresponding decrease in pulse intensity. The pulse energy is then safely increased through one or more stages of amplification, with the positive dispersion from optical elements in the amplifiers being negligible compared to the chirp imparted by the stretcher. Following amplification of the stretched pulses to high-energy, a compressor stage (see right inset in Fig. 1.3) is used to return the pulses to their original duration. As described above, a compressor compensates for the positive dispersion of the stretcher by imparting an equivalent negative dispersion on the pulses through similar use

of diffraction gratings. Depending on the bandwidth of the pulses after amplification, the pulse duration can be compressed to nearly the same value as the original oscillator output.

By the 1990s, mode-locked femtosecond sources based on solid state materials became more readily available. With matched grating stretchers and compressors, the rapid adoption of the CPA system architecture for the development of high energy ultrafast lasers followed. This resulted in a new class of ultra-high peak power femtosecond CPA laser systems, most often based on Ti:Sa gain materials. One disadvantage of Ti:Sa systems is the complex pumping scheme which in many cases involves the frequency-doubled output of multiple flash lamp pumped Nd:Glass amplifiers. While these systems are well suited for generating very high peak power ultrafast pulses, they suffer in terms of operation at high repetition rate for scaling average power. This has led to the development of modern diode pumped solid state lasers and to the investigation of other gain media.

1.2 Scaling Ultrafast Lasers to High Average Power

The development of ultrafast laser systems capable of high pulse energies at high repetition rates is an active and important area of laser research. As mentioned above, the peak power level of modern lasers has grown by many orders of magnitude in the last three decades. Progress in high average power lasers with high pulse energy has been more recent; being motivated by potential applications in science, medicine, defense, and industry. The development of modern diode lasers has been critical in this respect.

Historically, lamps were the primary method for pumping solid-state lasers due to their high peak powers and low cost. Following a period of decline when gas and dye lasers were more prominent, technological advancements led to a renewal of interest in solid state lasers by the 1980s [7]. Specifically, developments in material science and the arrival of powerful semiconductor laser diodes initiated this shift. The realization of powerful ultrashort pulse lasers occurred during this resurgence in solid-state laser development. For operation at high average power, the pumping efficiency and thermal management are two of the most important challenges. There are a number

of potentially detrimental thermo-optic effects to consider when operating at high power. The advent of diode pumping has allowed ultrafast solid state lasers to scale to high repetition rates with high pulse energy.

1.2.1 Diode Pumped Solid State Lasers

The viability of semiconductor laser diodes for pumping solid state lasers was first studied in the 1960s [16, 17]. Though their use at the time was deemed impractical and cost prohibitive, researchers noted that future developments would likely change this outlook. Since achieving greater commercial availability starting in the 1980s, powerful laser diodes have been adopted as ideal sources for pumping solid state lasers. Compared with flash lamps, laser diodes have several advantages that allow for more compact and efficient pumping schemes.

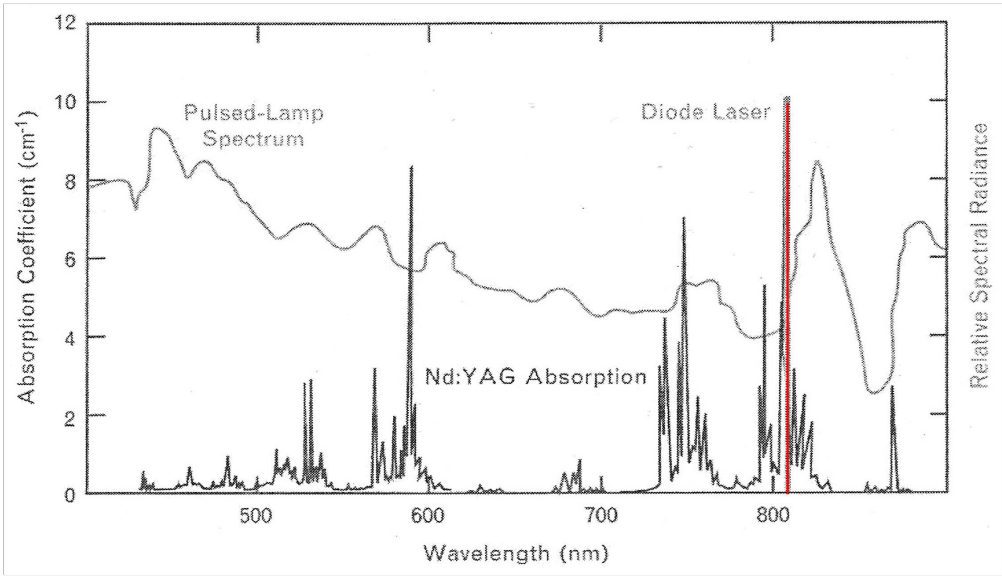

Figure 1.4: Overlayed spectra for Nd:YAG absorption, flash lamp pump emission, and diode laser emission. (From [18])

The implementation of diode pumping has considerable benefits for the efficiency of a solid-state laser system. As shown in Figure 1.4 above, flash lamps are inherently inefficient pump sources that emit a broad spectrum of light, of which only a small percentage is typically absorbed by the gain medium. As a result, most of the pump power contributes to heating the material and

thermal loading. For scaling to high average power, this represents a major limitation. Therefore, the monochromatic output of laser diodes is one of their most important characteristics for developing efficient high power solid-state lasers. This advantage allows materials with strong absorption peaks to be pumped at very high optical conversion efficiencies, with wall-plug efficiencies of >70% reported [19]. Powerful near infrared diodes offering linewidths of less than 5 nm have been developed with emission wavelengths matched to the absorption bands of common rare earth ions such as trivalent neodymium (Nd^{3+}) and ytterbium (Yb^{3+}).

In addition to these spectral advantages, modern laser diodes offer greater pumping versatility than flash lamps. Their coherent emission can be shaped and directed into the gain medium, allowing for novel pump schemes to be developed. This feature makes efficient alignment of the pump and seed beams possible, improving overall beam quality. The electrical characteristics of laser diodes also allow for prolonged operation at repetition rates beyond 1 kHz, while flash lamps are limited by the charging time of their power supplies. Additionally, modern diodes are engineered to be very compact while still offering high performance. The powerful pump diodes discussed in the next chapter produce 6 kW of peak power from 60 bars stacked together in a 5" x 3" x 0.75" package, while also maintaining output stability with effective water cooling.

1.2.2 Rare Earth Ion-Doped Materials

The materials in solid state lasers are typically glass or crystal hosts which have been doped with a small amount of an active impurity, often rare earth or transition metal ions. Important spectroscopic properties of these dopants include the upper-level lifetime, stimulated emission cross section, and gain bandwidth. For scaling a system to high pulse energy at high repetition rates, the upper-level lifetime is particularly important. This is especially true for diode pumping, since the relatively low peak power of diodes requires materials capable of storing high energy densities. The qualities of the host material are equally important, with careful consideration being given to optical, mechanical, and thermal properties.

In the 1960s, trivalent rare earth ions were identified as ideal dopants for use in crystals and glasses due to their favorable spectral qualities [20]. These ions exhibit a wide range of strong laser transitions typically characterized by four-level structures with long upper-level lifetimes. Common examples include neodymium (Nd^{3+}), erbium (Er^{3+}), thulium (Th^{3+}), and ytterbium (Yb^{3+}). The first of these dopants to be used in a laser was Nd^{3+}, which is by far the most popular rare earth ion in solid state lasers. The Nd^{3+} ion has several advantages for both flash lamp and diode pumping, including a low pump threshold at room temperature, strong absorption lines, and multiple fluorescent transitions [21]. In 1964 the ideal host material for Nd^{3+}, yttrium aluminum garnet (YAG), was demonstrated [22]. This synthetic garnet boasts excellent mechanical, thermal, and spectroscopic properties for use with high power diodes. The sharp absorption peak at λ = 808 nm for Nd:YAG made it ideal for pumping with InGaAsP and GaAlAs diodes which were developed early on. More recently, the availability of high power InGaAs diodes that emit at λ = 940 nm has renewed interest in Yb^{3+} doped materials.

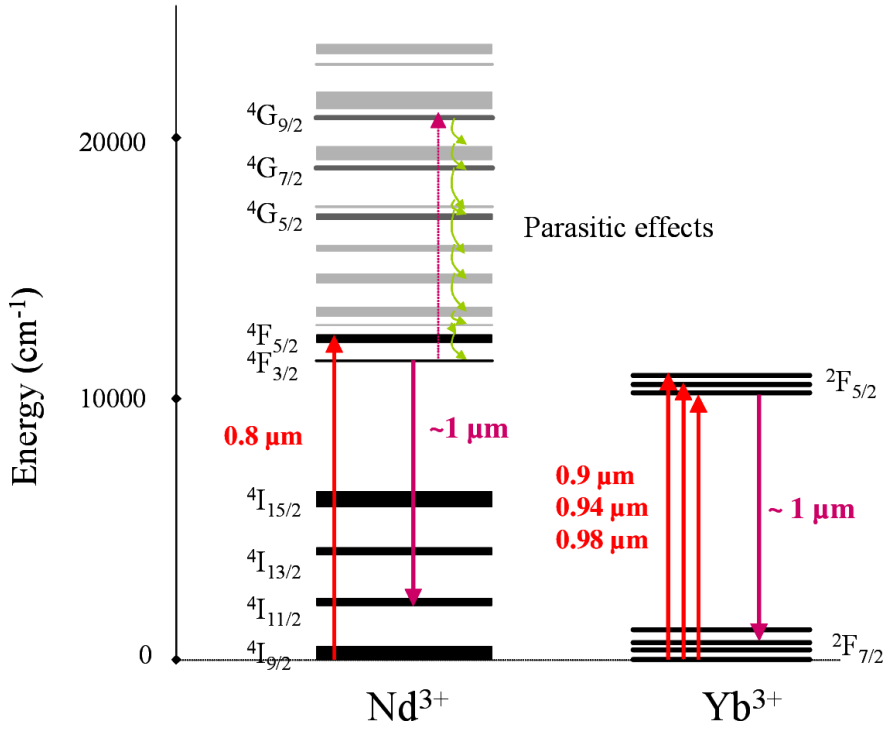

Figure 1.5: Comparison of the energy level structures of Nd^{3+} and Yb^{3+} with relevant pumping (up arrow) and lasing (down arrow) transitions. The potential for parasitic effects from the upper levels of Nd^{3+} is also indicated. (From [23])

Though Yb^{3+} was first identified and tested as a dopant in the 1960s [20], it was largely ignored in favor of Nd^{3+}. For both flash lamp and early diode pumping, this was due to several spectroscopic properties of Yb^{3+} doped materials. At room temperature, the lower laser level of Yb:YAG is very close to the ground state, as seen in Figure 1.5. This causes the lower level to be thermally populated by the ground state, creating a quasi-three level structure. From the Boltzmann distribution, the thermal population of the lower level in Yb:YAG is 5.5% at room temperature [7]. As a result, the pump power necessary for population inversion is increased, leading to a decrease in efficiency. For this reason, the four-level structure of Nd:YAG is preferred. Additionally, the stimulated emission cross section for Yb^{3+} doped materials is low compared with Nd^{3+}, resulting in a higher saturation fluence. For effective energy extraction in a Yb^{3+} doped amplifier, the laser fluence needs to exceed this high saturation fluence, increasing the likelihood of damage to optical elements. This property will be elaborated on further, in the next section.

Despite these properties, the advantages of Yb^{3+} doped materials far outweigh the drawbacks for high power diode pumping. The energy level diagrams in Figure 1.5 show that lasing occurs at ~ 1 μm between the ${}^2F_{5/2}$ and ${}^2F_{7/2}$ levels for Yb^{3+} and between the ${}^4F_{3/2}$ and ${}^4I_{11/2}$ levels for Nd^{3+}. For minimizing thermal effects from excess heat generation, particularly when scaling to high average power at high repetition rates, Yb^{3+} also benefits from a simple electronic structure. The two-manifold configuration prevents parasitic effects including excited-state absorption, upconversion, and cross-relaxation. These effects reduce conversion efficiency and deposit heat into the gain material. The energy level structure of Nd^{3+}, on the other hand, has many upper levels and can easily suffer from these effects at high pump energies; in addition to nonradiative decay of the upper-level population. Materials doped with Yb^{3+} also tend to have uniquely long upper-level lifetimes compared with alternatives such as Nd^{3+} [23]. For example, the 1030 nm transition in Yb:YAG has an upper-level lifetime of 950 μs. This is over four times longer than the 230 μs lifetime of the 1064 nm transition in Nd:YAG. The longer lifetime provides excellent energy storage with long pump pulses from low peak intensity diodes.

Another advantage of Yb^{3+} materials like Yb:YAG is the reduced thermal load when pumping at high power. The primary source of heat for an optically pumped gain material is the difference in photon energy between the pump and the laser emission, called the quantum defect. For Yb:YAG lasing at 1030 nm and pumped by 940 nm, this defect is only 9%. This is significantly smaller than other materials like Nd:YAG and Ti:Al_2O_3 which have quantum defects of 24% and 34%, respectively. Additionally, the absorption bandwidth of Yb:YAG at room temperature when pumped at λ = 940 nm is 18 nm compared with 2 nm for Nd:YAG pumped at λ = 808 nm. The broad bandwidth makes thermal management of the diode less restrictive on maintaining stable and efficient pump operation. This is especially important when operating at high repetition rates.

Finally, Yb^{3+} is better suited for doping in crystals like YAG and YLF than Nd^{3+}. The size of the Yb^{3+} ion is well matched with the Y^{3+} ions it replaces in the crystal lattice structure, allowing for high doping concentrations [24]. For Nd^{3+}, the difference in size limits doping concentrations to 1.5% or less to avoid concentration quenching which lowers the upper-level lifetime. The higher doping concentration also helps to minimize the impact of the relatively small absorption cross section of Yb:YAG. This advantage means Yb:YAG can be grown in various geometries, such as thin disks and slabs, while maintaining favorable optical quality and spectral characteristics. In the next section, the change in the properties of Yb:YAG when cooled to cryogenic temperatures are discussed, further demonstrating the value of Yb:YAG for high average power operation.

1.2.3 Yb:YAG at Cryogenic Temperature

From the discussion above, it is clear why Yb^{3+} has become widely used as a dopant for scaling diode pumped systems to high average power, particularly in yttrium aluminum garnet ($Y_3Al_5O_{12}$ or YAG). The exceptional properties of YAG as a host material have been known for decades, as previously mentioned. Compared with other solid state laser host materials, YAG is one of the hardest and the cubic crystal structure makes it optically isotropic. With the benefit of extensive development of YAG in Nd:YAG lasers, and the advantage of the high doping concentrations possible with Yb^{3+}, commercially available Yb:YAG crystals can be grown in a range of sizes

with high quality. As a result, high average power operation at room temperature has been achieved with diode pumped Yb:YAG lasers. However, the important properties of Yb:YAG for high power operation become even more advantageous when the material is cooled to cryogenic temperatures [25]. These mechanical, spectral, and thermo-optic improvements are summarized later in this section in Table 1.1.

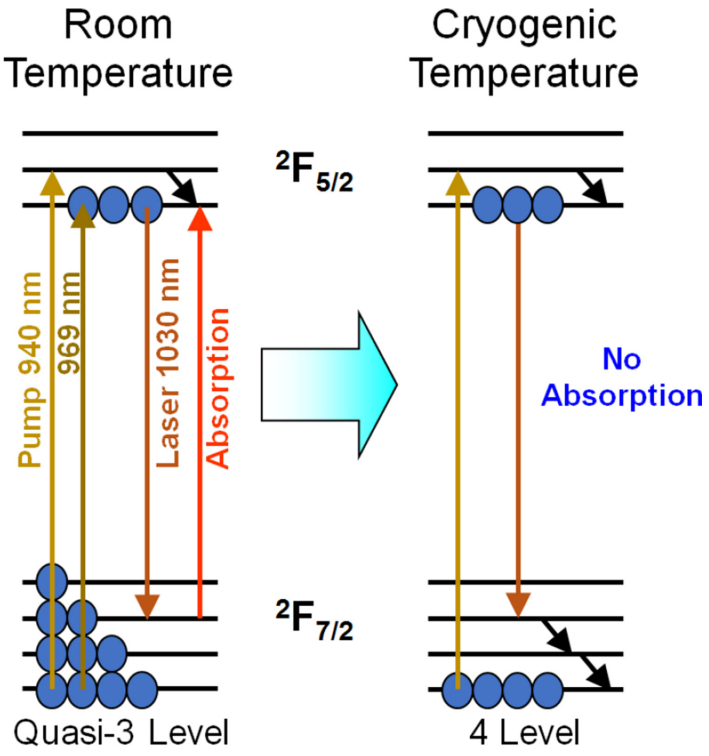

Figure 1.6: The transition from a quasi-three level to a four-level laser system in Yb:YAG between room temperature (300 K) and cryogenic temperature (77 K). (From [26])

The disadvantages of the quasi-three level structure of Yb:YAG at room temperature have been described. One of the most notable results of cooling to cryogenic temperatures is the depopulation of the lower laser level. The thermal population is reduced to a negligible level, effectively making Yb:YAG a four-level laser [27]. This change causes the pump threshold to decrease as well as significantly increasing the emission cross section. The saturation fluence is a critical value for efficient operation at high average powers, as mentioned previously. At room temperature, the

saturation fluence of Yb:YAG is 9.2 J/cm^2 [7]. Though the properties of Yb:YAG relative to Nd:YAG make it less susceptible to the adverse effects of thermal loading, optical damage is still a concern at room temperature. The saturation fluence is inversely proportional to the stimulated emission cross section. Therefore, the dramatic increase in the cross section at 77 K results in a corresponding decrease in the saturation fluence. By reducing the required saturation fluence at cryogenic temperatures to 20% of the room temperature value, the risk of damage is severely mitigated and efficient energy extraction can occur.

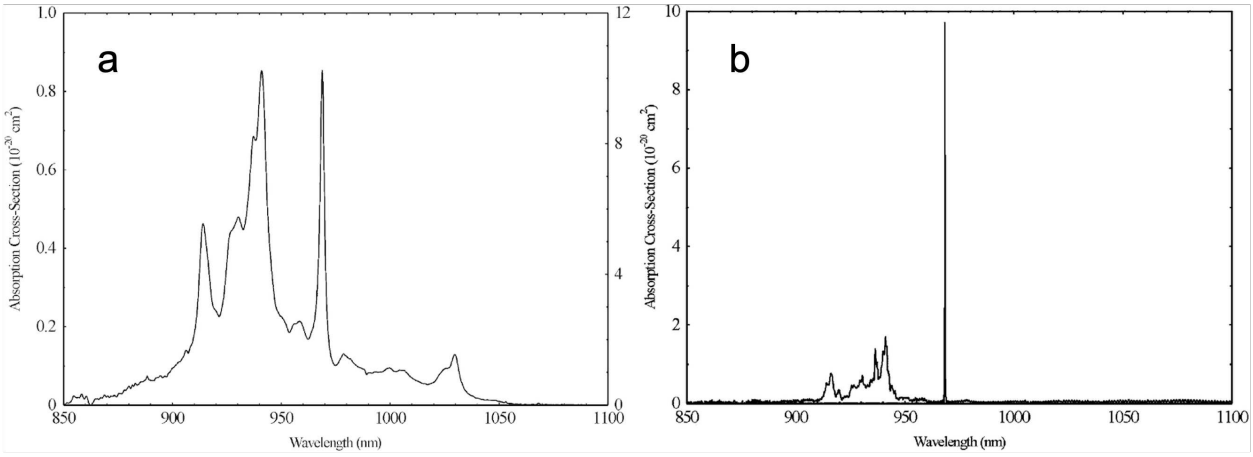

Figure 1.7: The absorption cross section of 9.8 at.% doped Yb:YAG for a) room temperature (300 K) and b) cryogenic temperature (75 K). (From [28])

There is also a large increase in the absorption cross section at 77K, as seen in Figure 1.7 above, further improving efficiency and reducing negative thermal effects due to heating [27]. A noteworthy side effect of cryogenic cooling is the bandwidth narrowing which limits the pulse duration that can be achieved. For Yb:YAG at room temperature, the emission linewidth is $\sim$5 nm (FWHM) at 1030 nm which can support pulse durations on the order of several hundred femtoseconds. As a result of the narrowing at 77 K, the linewidth is reduced to less than 1 nm, corresponding to a minimum pulse duration of several picoseconds.

Table 1.1: Changes in the properties of Yb:YAG when cooled from room temperature (300 K) to cryogenic temperature (77 K). (From [27–32])

Yb:YAG Properties	300 K	77 K	Factor
Thermal Conductivity (W/m*K)	8.6	60	x7
Thermo-Optic Coefficient (10^{-6}/K)	7.8	0.9	x1/8
Expansion Coefficient (10^{-6}/K)	6.14	1.95	x1/3
FWHM Emission Bandwidth (nm)	9	1.5	x1/12
Stimulated Emission Cross Section (10^{-20}cm^2)	2.1	11	x5
Saturation Fluence (J/cm^2)	9.2	1.7	x1/5

Besides the spectroscopic changes to Yb:YAG at cryogenic temperatures, there are also important thermo-optic improvements to the material, as seen in Table 1.1 above. Adverse temperature effects such as thermal lensing and thermally induced birefringence limit the ability to scale systems to high energy operation at high repetition rates. These effects are inversely proportional to the thermal conductivity of the gain material. In the case of an end-pumped laser rod [7], the temperature distribution is parabolic:

$$T\left(r\right) = T\left(r_0\right) + \frac{Q}{4K}(r_0^2 - r^2) \tag{1.15}$$

when assuming uniform heating along the rod. Where K is the thermal conductivity, Q is the heat density, r is the radial position, r_0 is the radius of the rod, and T is the temperature. The thermal conductivity is then inversely related to the temperature along the rod. For a constant thermal conductivity K with temperature, the refractive index within the rod, $n(r)$, can be expressed as:

$$n\left(r\right) = n_0 + \Delta n_t(r) + \Delta n_s(r) \tag{1.16}$$

where $\Delta n_t(r)$ and $\Delta n_s(r)$ are thermal gradient and mechanical stress contributions, respectively, to the refractive index. A beam traveling along the rod experiences a lensing effect due to

the induced parabolic distribution of the index being highest at the center. As such, the factor of 7 improvement of the thermal conductivity to 60 W/m*K at liquid nitrogen temperature is significant. Though it is important to note that this value decreases with increasing doping concentrations. Additionally, the thermo-optic coefficient, which is the derivative of the index of refraction with respect to temperature and a contributor to Δn_t, decreases by a factor of 8 at cryogenic temperature. Finally, mechanical stress in the material contributes to thermal lensing based on the contribution of the thermal expansion coefficient to the index change. The reduction in the thermal expansion coefficient of Yb:YAG at cryogenic temperatures is 1/3 of the original value. The changes seen in these three properties serve to significantly mitigate the effects of thermal lensing in Yb:YAG at cryogenic temperatures.

1.2.4 Current Status of High Average Power, High Pulse Energy, Diode-Pumped Lasers

The documented advantages of Yb^{3+} for diode pumped lasers, described above, has led to development of powerful systems in recent years. Figure 1.8 below shows the results of various Yb^{3+} based lasers in terms of repetition rate, pulse energy, and average power. These results cover a range of designs and crystal geometries. In the context of this thesis, the current state of diode pumped Yb:YAG lasers for high energy (mJ to J), high repetition rate (kHz scale), and short pulse (ps) operation is of primary interest.

The thin disk geometry for Yb:YAG crystals was first demonstrated in the 1990s and has since become a successful design for high power short pulse amplifiers [56, 57]. The setup consists of a Yb:YAG disk in the range of 100-300 μm thick and up to 1.5 cm in diameter. The properties of Yb:YAG, as mentioned above, enable high quality crystal growth at these dimensions while also permitting favorable doping concentrations. The crystal is coated on both sides for the pump and seed wavelengths; with the front surface coating being antireflective (AR) and the back surface being highly reflective (HR). In this configuration, the crystal is known as an "active mirror" since the crystal itself is coated to reflect both the pump and seed beams. The main concern for this

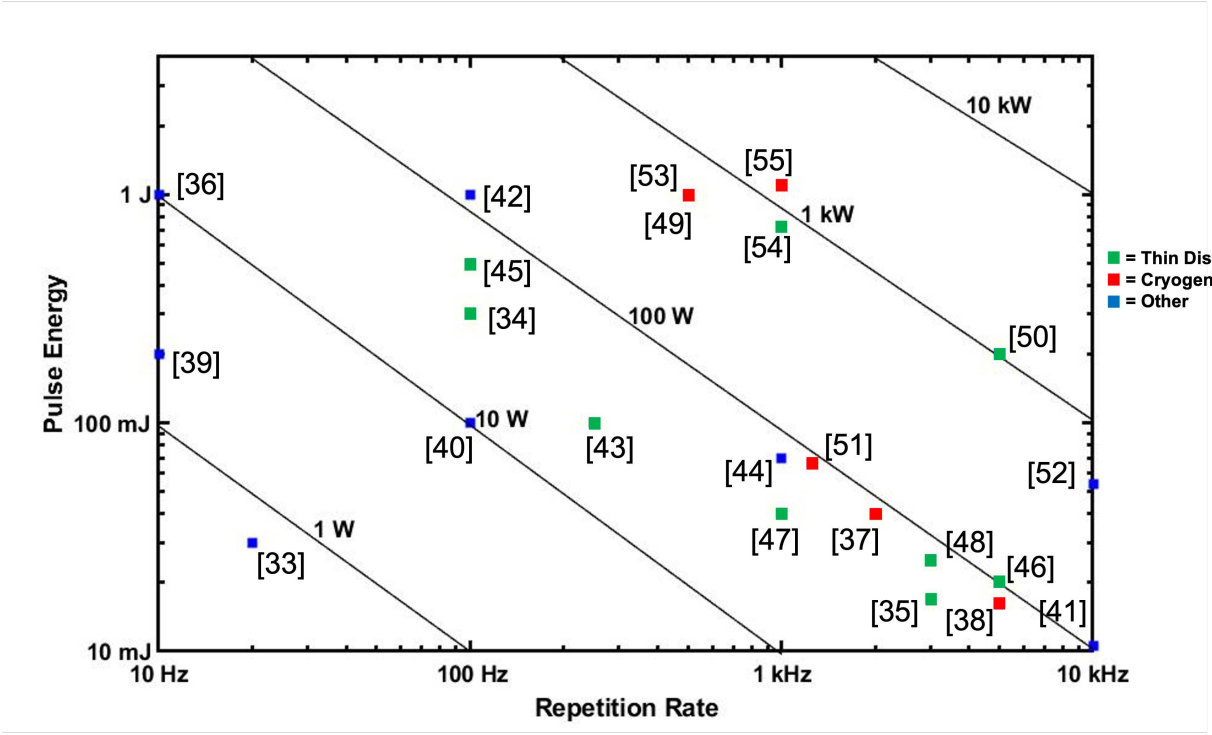

Figure 1.8: Plot of current performance of Yb^{3+} lasers with pulse energy >10 mJ and repetition rates >10 Hz. Ref. numbers listed [33–55]

geometry is effective cooling of the crystal, given the small volume and high pump threshold at room temperature. This typically involves bonding the back surface (HR) of the crystal to a water-cooled copper-based heatsink. The success of this design is due to the large cooling area of the crystal relative to the volume, which allows for effective thermal management. Small temperature gradients in the direction of beam propagation mean that thermo-optic effects are minimized. For further thermal efficiency, thin-disk systems can utilize pumping at the zero-phonon line (ZPL) of Yb:YAG at 969 nm. In this scheme, the upper laser level is pumped directly, resulting in a reduction of thermal loading by 32% [58]. The drawback of this method is the narrow bandwidth at 969 nm of 1-2 nm. This necessitates expensive volume Bragg grating-stabilized pump diodes in order to operate at high power. Despite this, the commercial availability of kW-class VBG diodes and ZPL-pumped thin disks reporting up to 80% optical efficiency make this a viable option for scaling to high average power [59].

Thin disk Yb:YAG lasers with pulse energies up to 300 mJ have been reported from regenerative amplifiers [60]. In 2017, Nubbemeyer et al reported 1 kW of average power from a Yb:YAG thin disk regenerative amplifier CPA system [50]. This design utilizes a dual thin-disk, ring type resonator cavity for the main amplifier. By ZPL pumping with multi-kW diodes, the 1 mJ seed is amplified to pulse energies of 100-200 mJ at 5-10 kHz repetition rates. After compression, a pulse duration of 1.1 ps is achieved. Recently, commercial regenerative amplifiers based on Yb:YAG thin disks have become available offering pulse energies >200 mJ at 1 kHz [61]. One such system has been utilized to seed a multi-pass CPA laser based on thin-disk amplifiers. This system demonstrated 1 ps compressed pulse energies of 720 mJ at 1 kHz repetition rate [54]. The thin-disk Yb:YAG geometry has shown success at achieving high average power with high pulse energies, however further scaling at room temperature is a challenge.

The highest energies for kHz-level compressed pulses have been generated by cryogenically cooled Yb:YAG lasers. The benefits of cryogenically cooled Yb:YAG, outlined above, enable scaling to such high pulse energies. Due to the bandwidth narrowing effects at cryogenic temperatures, the use of a broadband material in the front end of the system is common. This "hybrid" setup allows for a higher bandwidth before amplification in the cryogenically cooled stages, minimizing the effects of narrowing on the final pulse duration. The cryogenically cooled Yb:YAG CPA laser developed at the Advanced Beam Laboratory (ABL) at Colorado State University (CSU) has reported a record 1.1 J pulse energy for 4.5 ps compressed pulses at 1 kHz repetition rate, or 1.1 kW average power operation [55]. This system is reviewed in greater detail in Chapter 2 of this thesis.

1.2.5 Applications

The development of high-energy diode pumped lasers with short pulse durations at high repetition rates has enabled a number of applications. Such applications include driving soft x-ray laser sources [42, 49, 62–64], developing optical parametric chirped pulse amplifiers (OPCPA) [65–68], and pumping high repetition rate femtosecond lasers by frequency doubling [69, 70]. These systems have also served to develop secondary sources of high energy photons [71–73] and parti-

cles [74–76]. In addition, there are a number of defense and industrial applications. Of particular interest is the propagation in air of such high peak power, high energy, ultrafast pulses. This regime leads to a self-sustaining process called filamentation, wherein the beam self-focuses and forms a plasma channel during atmospheric propagation. Potential applications of this phenomenon include weather control [77] and laser-guided lightning discharges [78]. For these reasons, active research continues for the development of laser systems in this class.

1.3 High Power Laser Propagation in Air: Filamentation

The propagation of intense laser pulses through various media has been studied since the 1960s. In particular, the interaction of such pulses with atmospheric air is of keen interest. With the advent of ultrafast lasers, the available peak power of laser pulses was significantly increased. This new class of lasers revealed a process by which pulse propagation is heavily affected by nonlinear interactions, leading to the discovery of filamentation. This regime is characterized by a highly intense, narrow beam which is partially ionized and capable of sustaining its dimensions over long distances. Since Braun et al first demonstrated this process in air [79], the physical processes and conditions affecting the formation of filaments have been extensively studied [80, 81].

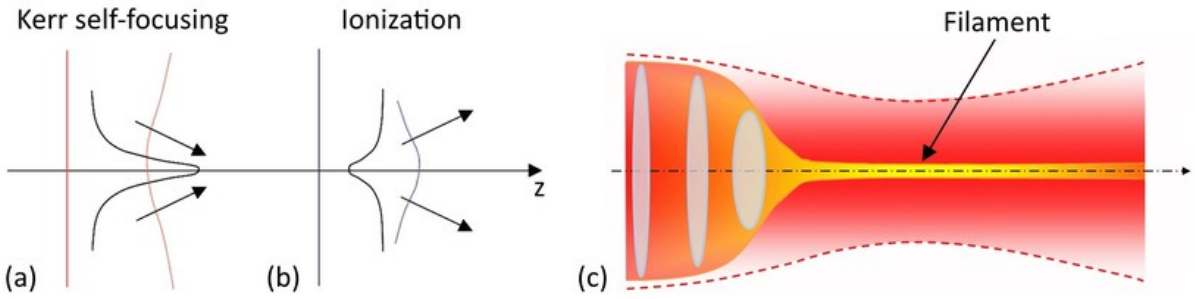

Figure 1.9: The filamentation process begins with a) focusing of the beam due to the optical Kerr effect, followed by b) plasma defocusing of the beam due to ionization, c) which results in the formation of a filament. (From [82])

In general, filamentation is a dynamic nonlinear interaction between a highly intense beam and the medium it is propagating through, including solids, liquids, and gases. The primary effects

which drive atmospheric filamentation are self-focusing of the beam by the optical Kerr effect and the counter-balancing effect of plasma defocusing due to photoionization of the air which causes the beam to refract. For a Gaussian beam, the propagation distance is normally limited by diffraction to the Rayleigh length. In order for filamentation to occur, the beam must be of high enough intensity to overcome diffraction. The optical Kerr effect is the nonlinear response of a material's refractive index to an intense electromagnetic field. The index of refraction of air, n, depends on the intensity of an electromagnetic field according to:

$$n = n_0 + n_2 I\left(r, t\right) \tag{1.17}$$

where n_0 is the index for a given wavelength, n_2 is the nonlinear index of refraction of the medium and $I(r, t)$ is the field's intensity dependent on time and position. For a Gaussian beam, the center is the point of highest intensity and will therefore propagate through a higher index which causes wavefront distortion and convergence of the beam, similar to a lens. At high enough intensity this effect can overcome diffraction, leading to a collapse of the beam known as self-focusing. The threshold for self-focusing to occur is the critical power given by [83]:

$$P_{cr} = a\frac{\lambda_0^2}{4\pi n_0 n_2} \tag{1.18}$$

where λ_0 is the wavelength and a is a constant which is dependent on the transverse beam profile. The required input power to exceed this threshold in a gas is typically several GWs. With the high intensity of femtosecond pulses, self-focusing of a beam is easily achieved with low pulse energies. For example, a Ti:Sa laser (λ = 800 nm) producing 100 fs pulses will exceed the 3.2 GW critical power to self-focus with a pulse energy of just 0.4 mJ [80]; while for a Yb:YAG laser (λ = 1030 nm) the 5.3 GW critical power is reached for 7 ps pulses with 37 mJ of energy.

The subsequent plasma defocusing of the beam is caused by photoionization of the air; either by multiphoton or tunneling ionization. As the beam collapses due to self-focusing, the intensity increases until ionization of air molecules occurs. The resulting plasma causes the index of

refraction to decrease according to:

$$n\left(r,t\right) = n_0 - \frac{\rho\left(r,t\right)}{2\rho_c} \tag{1.19}$$

where $\rho\left(r,t\right)$ is the free electron density and ρ_c is the critical plasma density above which the plasma becomes opaque, given by $\rho_c = \epsilon_0 m_e \omega_0^2 / e^2$ (ϵ_0 is the vacuum permittivity, m_e and e are the electron mass and charge, and ω_0 is the angular frequency). As the pulse propagates, the leading portion generates the plasma which defocuses the trailing portion. This decrease in the refractive index is the negative lens effect which counters the collapse of the beam due to self-focusing from the optical Kerr effect.

The balance achieved between these two processes is the primary mechanism driving filamentation, though there are other factors involved [80]. The sustained focusing and defocusing of the beam forms the highly intense filament channel which is capable of propagating for long distances [84]. The unique properties of filamentation have inspired development of new applications as well as adaptation to existing applications, as detailed in [80, 81]. The use of filaments for remote sensing applications has been an area of interest since their discovery. These include remote sensing from terahertz generation and detection, LIDAR by filament generated supercontinuum, and filament-induced breakdown spectroscopy. Other applications include atmospheric research, and formation of waveguiding structures for optical and radio frequencies. Most relevant to the topic of this thesis is the use of filamentation to guide electrical discharges in air.

1.3.1 Filament-Guided Electrical Discharges in Air

Since the 1970s, research has been conducted on the potential for electrical discharges, such as lightning, to be triggered and guided by ionization from the propagation of intense laser pulses [85]. For such discharges to occur in the atmosphere, a localized electric field of sufficient strength to induce ionization is required. In the traditional picture of high-pressure discharge formation, the resulting avalanche process creates outwardly propagating plasma streamers which combine to form a self-sustaining leader in the direction of the opposite charge [77]. The resulting channel

allows a rapid flow of current, forming a discharge. By focusing an intense optical field between electrodes, the resulting ionization can initiate this process at a faster rate. In the past, high energy nanosecond lasers were used to generate this plasma [86]. However, the long pulse durations prevented the peak power necessary for filamentation to occur as described above. Instead, an optically opaque and discontinuous plasma channel forms due to the high densities from avalanche ionization, as shown in Figure 1.10a below. While the ability to trigger and guide discharges was successfully demonstrated, long distance propagation was limited. Interest in this application for intense lasers continued into the 90s, when the rapid proliferation of ultrafast lasers led to the discovery of filamentation.

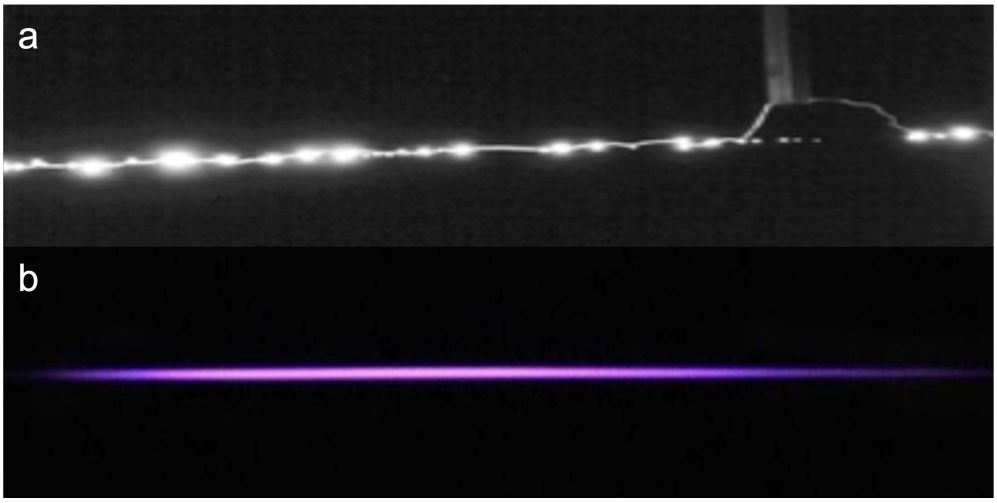

Figure 1.10: Intense laser pulse propagation: a) nanosecond pulses form a discontinuous chain of dense plasma balls (From [87]), while b) ultrafast pulses form a continous, weakly ionized filament.

The current state of filament-guided discharges consists of ongoing research into the dynamics of the process under different experimental conditions. There has also been significant discussion on the primary mechanisms by which filaments trigger and guide discharges. In particular, the causes of the reduction in voltage required for dielectric breakdown to occur are of interest. Initially, the weakly ionized plasma left in the wake of the pulse, as shown in Figure 1.10b, was seen as an ideal conductive "wire" between electrodes. However, the relatively low electron density and short recombination time typically make sustained discharges over long distances challeng-

ing. The formation of streamers and leaders, akin to natural lightning, have been observed. It has been suggested that these play an important role for initiating breakdown [88, 89]. Though, other research has demonstrated discharge formation in the absence of streamers [90, 91]. A commonly cited mechanism for discharge is the hydrodynamic response of the gas following filament formation [92]. The resulting density depression has been reported as the primary source of reduction in the breakdown voltage necessary to trigger discharges [93]. The variability of the discharge process due to experimental parameters has motivated ongoing efforts to study the effects of different pulse energies, repetition rates, and pulse durations [91, 94, 95].

The majority of research has been conducted with femtosecond pulse durations at low repetition rates. More recently, picosecond filamentation has been studied and a reduction in breakdown voltage compared with fs pulses has been reported [91], while for high repetition rates a cumulative hydrodynamic response is suggested to further reduce breakdown voltage [96]. The results of triggering and guiding discharges with high energy ps pulses at up to 1 kHz repetition rate are detailed in Chapter 3 of this thesis.

1.4 Outline of Thesis Content

The content of Chapter 2 describes the kW-class, cryogenically cooled Yb:YAG laser system at the CSU Advanced Beam Laboratory (ABL). The system layout from the mode-locked oscillator to the multiple stages of amplification before final pulse compression is described. The developmental challenges of scaling this system and the modular design are also discussed. Finally, the demonstrated performance of the system producing 1.1 J, 4.5 ps pulses at 1 kHz repetition rate are presented.

Chapter 3 details the application of the Yb:YAG laser system to the guiding of electrical discharges. The successful generation of filamentation of the laser pulses and the subsequent guiding of electrical discharges at high repetition rate is presented. Lastly, the physics of the filament formation and discharge initiation using $\lambda = 1030$ nm pulses of up to 250 mJ and picosecond duration at repetition rates up to 1 kHz are discussed.

Chapter 2

kW-Class Diode Pumped Yb:YAG Laser

2.1 Introduction and System Overview

This chapter covers the diode-pumped CPA laser system developed at CSU's Advanced Beam Laboratory, including the design and performance. The following chapter describes the use of this laser to study the generation and guiding of electrical discharges in atmospheric air by high energy picosecond laser pulses at repetition rates up to 1 kHz. This laser system uses a cryogenically cooled active mirror Yb:YAG multi-pass amplifier architecture that is capable of producing compressed pulses of 1.1 J at 1 kHz [55], giving 1.1 kW of average power. The performance capabilities and design of this system has allowed it to be utilized for applications such as soft x-ray generation [62], frequency-doubled pumping of ultrashort pulse lasers [69], filamentation experiments [97], and guiding of electrical discharges (Chapter 3 of this thesis).

A diagram of the kW average power system layout is shown in Figure 2.1. This compact system fits on a single 5' x 12' optical table. The front end makes use of a passively mode locked diode-pumped Yb:KYW oscillator from which low energy femtosecond pulses are stretched in a grating stretcher prior to amplification. The stretcher takes nJ-level, sub-picosecond pulses and stretches them to several hundred picoseconds. These stretched pulses then seed a room temperature Yb:YAG thin-disk regenerative amplifier. The amplified pulses have millijoule-level energy at 1 kHz repetition rate. Prior to further amplification, a Pockels cell between two cross-polarized calcite crystals is used to improve pulse contrast and prevent feedback. After the laser front end, there are two cryogenically cooled Yb:YAG power amplifiers in which the pulses are amplified through an active mirror multi-pass configuration to pulse energies > 1 J. Finally, the laser pulses are compressed by a dielectric grating compressor which matches the dispersion of the stretcher. The final output is 1.1 J of pulse energy at 4.5 ps duration for 1 kHz repetition rate. Each of the system stages are described below, along with the characterization of the laser output.

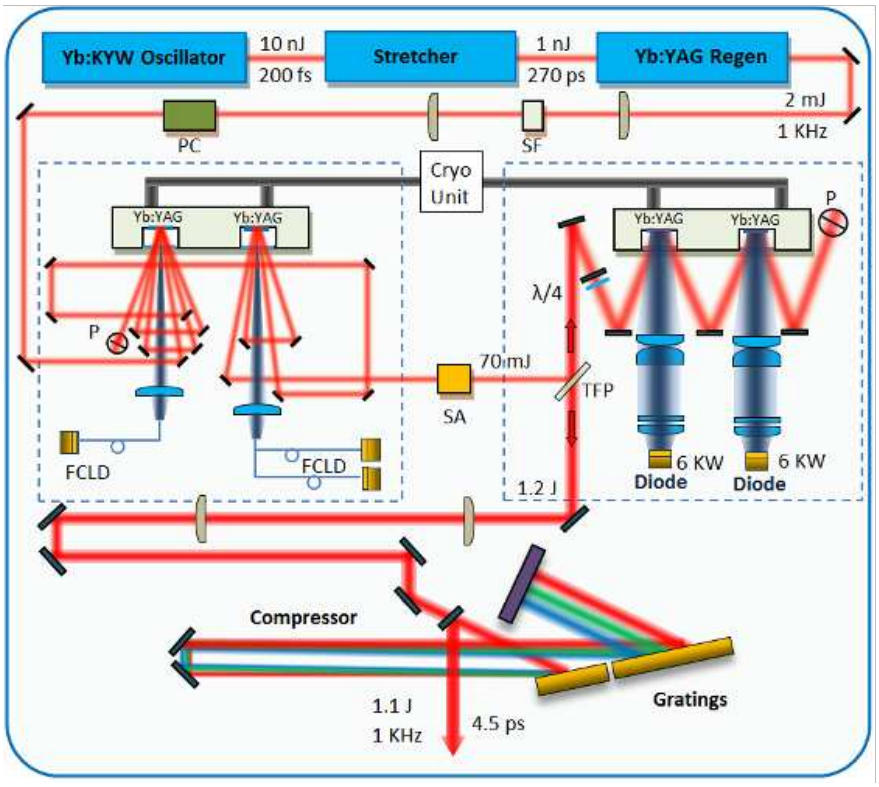

Figure 2.1: Kilowatt Yb:YAG CPA system diagram showing the various stages and the path of the pulses through the system. Regen = regenerative amplifier; SF = spatial filter; PC = Pockels cell; P = periscope; FCLD = fiber-coupled laser diode; SA = serrated aperture; TFP = thin film polarizer; $\lambda/4$ = quarter wave-plate. (From [55])

2.2 Passively Mode Locked Oscillator

The principles of operation and function of a mode-locked oscillator in the context of a CPA system was detailed in Chapter 1. The diode pumped Yb:KYW oscillator in this system utilizes a semiconductor saturable absorber mirror (SESAM) for passive mode locking. The SESAM promotes mode locking by reflecting a pulse of sufficient intensity, while less intense oscillations are suppressed through absorption, allowing for preferential amplification of a single pulse through the gain medium and eventually leading to mode locking [98]. This is accomplished by a material response to an optical intensity based on saturation of the material absorption which sets the threshold for the reflectivity to increase, as shown in Figure 2.2. Another important property for a SESAM is fast relaxation time allowing for rapid absorption recovery in order to prevent gain depletion from pulses below the saturation fluence threshold. The SESAM in the oscillator of this system is rated at 2% saturation loss, which is the percentage of loss for the more intense pulses at maximum reflectivity (saturated).

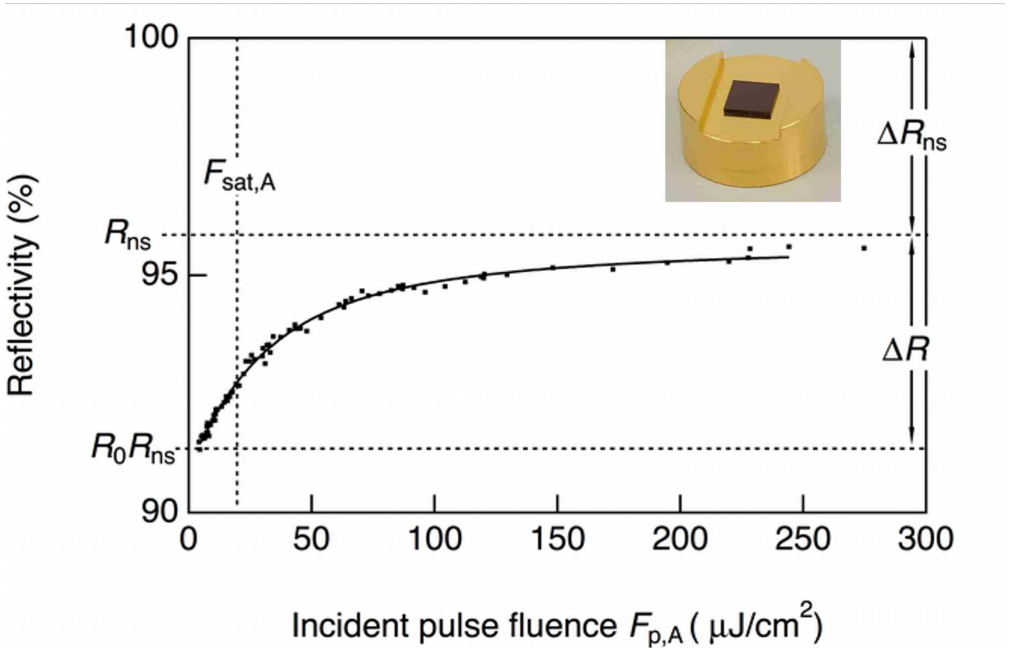

Figure 2.2: Reflectivity as a function of incident pulse fluence for a 5% loss SESAM, with inlaid image of typical commercial SESAM. (From [99])

The oscillator gain medium is a 5%-at ytterbium doped potassium yttrium tungstate (Yb:KYW) crystal measuring 5 x 5 x 3 mm. The benefit of a hybrid setup with a broad bandwidth front end material for cryogenic Yb:YAG amplifier based systems was mentioned in Chapter 1. For this purpose, Yb-doped double tungstates Yb:KYW and Yb:KGW are popular choices due to their broad gain bandwidth, high stimulated emission cross section, and low quantum defect [100]. The absorption and emission cross sections for Yb:KYW pumped at 981 nm are significantly higher than for Yb:YAG, and the broad bandwidth can support pulse durations of $\sim$100 fs [101]. Although the thermal conductivity of Yb:KYW is below Yb:YAG, the very low quantum defect of <6% and the ability to use relatively small crystals due to the favorable cross sections allows the thermal load when pumping Yb:KYW to remain low.

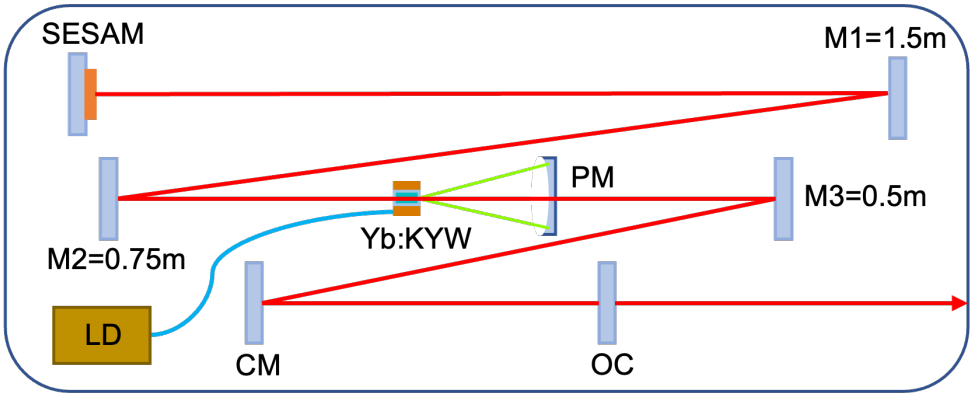

Figure 2.3: Schematic of the diode-pumped passively mode locked Yb:KYW oscillator. SESAM = semiconductor saturable absorber mirror; CM = chirped mirror; OC = output coupler; LD = laser diode.

For mode-locked oscillators generating ultrashort pulse durations, dispersion compensation within the cavity is necessary [102]. The broad bandwidth gain materials required for fs pulses are a source of positive dispersion for the pulses. A common method for compensating this dispersion within a SESAM mode-locked oscillator is to use a chirped mirror [7]. The layered structure of this mirror allows for differing penetration depths dependent on wavelength. The net result of this design is that the different wavelength components experience different group delay relative to one another. By carefully designing the layers of a chirped mirror, the broad spectral bandwidth of

the oscillator output pulses can be maintained. This is important, as reduced bandwidth increases the minimum possible pulse duration after compression. The chirped mirror used in this oscillator has a group delay dispersion (GDD) of -2000 fs^2 to cancel the positive dispersion from the crystal, covering a bandwidth of +/- 10 nm centered at 1030 nm.

The pump laser is a 30 W, 980 nm fiber-coupled diode with a 200 μm core which is 1:1 imaged onto the Yb:KYW crystal by a concave pump mirror (PM) with a radius of 101.6 mm. This is done by mounting the fiber end within the same water-cooled copper heatsink as the crystal, in an offset position. A hole drilled through the center of the pump mirror allows it to be positioned within the cavity, as seen in Figure 2.3. The SESAM is positioned as one of the cavity end mirrors with the other being an output coupler (OC) with 6% transmission. In addition to the chirped mirror (CM), three curved cavity mirrors (M1, M2, and M3) produce a mode matched spot on the crystal, as well as a focal spot on the SESAM which ensures sufficient fluence. The beam of mode-locked pulses leaving the cavity is several millimeters in diameter. The oscillator operates with an output of $\sim$0.6 W at a repetition rate of 55 MHz, or $\sim$11 nJ pulse energy. The output spectrum, shown in Figure 2.4 below, has a full width at half maximum (FWHM) bandwidth of 3.8 nm. Despite the center wavelength being offset from 1030 nm, the wide bandwidth allows amplification in subsequent Yb:YAG stages, as will be described in the next section on the pulse stretcher.

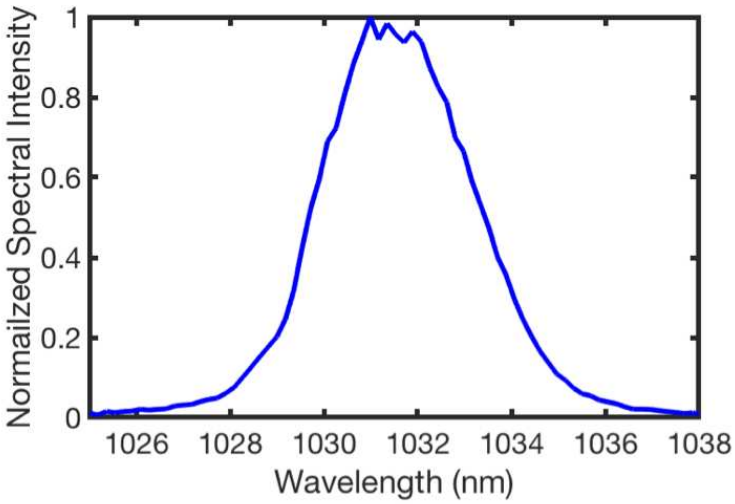

Figure 2.4: Output spectrum of the passively mode-locked Yb:KYW oscillator.

This Yb:YAG laser system may also be used as a frequency-doubled pump laser for a Ti:Sa laser. In this case, the CPA setup is unnecessary, as the upper-level lifetime of Ti:Sa is $\sim$3 μs, and high doubling efficiency can be achieved with nanosecond pulse durations. In this case the mode-locked oscillator is substituted by a pulse synthesizer based on a fiber-coupled diode laser and a computer controlled arbitrary waveform generator. The use of the arbitrary waveform generator allows for the seed pulses to be shaped in such a way that the output of the final amplifier has a square pulse shape [69]. This shape maximizes the doubling efficiency in an LBO crystal.

2.3 Pulse Stretcher

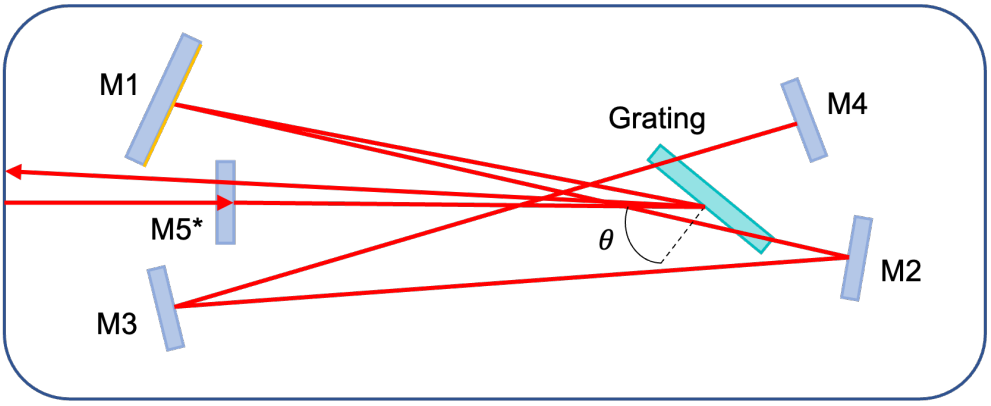

Figure 2.5: Folded Martinez-style grating pulse stretcher layout. M1 = gold coated spherical concave mirror; M2 and M3 = flat mirrors for extending path length; M4 = focal plane mirror; M5* = end mirror with spectrum-clipping mask.

The output pulses from the mode-locked Yb:KYW oscillator are sent through the pulse stretcher prior to seeding the regenerative amplifier. This CPA system uses dielectric gratings to stretch and compress the pulses in time. The stretcher is a Martinez type which produces positive dispersion, as described in Chapter 1 [15]. A folded mirror design allows for a more compact setup while also providing the multi-meter path length necessary for adequate dispersion. The traditional Martinez style stretcher is made up of two parallel gratings with a telescope in between to produce positive dispersion. In a folded design, the mirror arrangement allows the use of a single grating over which the beam passes four times. The oscillator pulses are incident at 56 degrees (θ_i) onto the dielectric

grating which has a line density of 1740 mm^{-1}. Instead of a telescope, a spherical concave mirror (M1) and a focal plane mirror (M2) provide the effective negative path for positive dispersion. An additional pair of mirrors (M3, M4) allows for the 2.5 m propagation between grating passes, while keeping the stretcher footprint confined. The end mirror (M5*) sends the beam back along the same path and enables the compact single grating, double pass design. After four passes on the grating, the pulses exit the stretcher along a different path due to it being intentionally misaligned.

The expression for the second order dispersion of a grating pair, Equation (1.14), was derived in Chapter 1. When expressed in terms of the angle of incidence, θ_i, the stretcher GDD can be calculated from [14]:

$$\frac{d^2\varphi}{d\omega^2} = -\frac{N\lambda^3 L}{2\pi c^2 d^2}\left[1-\left(\frac{\lambda}{d}-sin\theta_i\right)^2\right]^{-\frac{3}{2}} \tag{2.1}$$

where N is the number of passes, λ is the wavelength, L is the grating separation, d is the grating line density, c is the speed of light, and θ_i is the angle of incidence on the first grating. For the stretcher design in this system the grating separation is (effectively) -2.5 m, with a grating line density of 1740 mm^{-1}, and an incidence angle of 56 degrees. Therefore, a positive chirp, due to the effective negative path length after a double pass through the stretcher, of:

$$GDD \approx 1.51 \times 10^9\ fs^2 \tag{2.2}$$

is imparted onto the oscillator pulses. The chirped pulses of the stretcher seed a room temperature Yb:YAG regenerative amplifier followed by a pair of cryogenic Yb:YAG power amplifiers. The mismatch between the central wavelength and bandwidth of room temperature versus cryogenic Yb:YAG [103] has been addressed within the stretcher. After the first two passes across the grating, the pulses reflect off the end mirror which has a spectrum-clipping mask over it (M5* in Fig. 2.5). By blocking a portion of the light, the stretcher output spectrum is centered at 1030 nm. This compromise is carefully designed to allow for maximum energy while also maintaining broad bandwidth after the final amplification stage. The bandwidth after the regenerative amplifier is 0.46 nm FWHM due to gain narrowing. From [14], the variation of group delay with wavelength

for a grating pair results in a pulse duration, $\Delta\tau$, of:

$$\Delta\tau = \frac{L(\lambda/d)\Delta\lambda}{cd(1-(\lambda/d - sin\theta_i)^2)} \tag{2.3}$$

where L in this case is the total path length for the double pass setup, λ is the wavelength, d is the grating separation, c is the speed of light, θ_i is the angle of incidence, and $\Delta\lambda$ is the spectral bandwidth. The design of the stretcher in this system results in a stretched pulse duration of:

$$\Delta\tau \approx 330ps \tag{2.4}$$

With the pulse duration increased by a factor of >103 X, the pulses can now be safely amplified in the subsequent stages, where any further positive dispersion contributions are negligible [99].

2.4 Regenerative Preamplifier

The final stage of the laser's front end is the regenerative amplifier based on a room-temperature Yb:YAG thin disk. A regenerative amplifier is a type of multi-pass amplifier that uses an optical switch to trap pulses inside a resonator to pass across the gain material until gain saturation occurs [7]. This requires careful synchronization of the optical switch and pump source so that the seed pulses are coupled into the cavity and removed once amplification is maximized. Due to the extremely high gain of this amplifier configuration, around 10^6, there is also significant spectral gain narrowing that occurs. This motivates using the broader bandwidth offered by amplification in gain media at room temperature, in order to preserve bandwidth for the later compression stage. In this amplifier nJ seed pulses are amplified to 2 mJ at 1 kHz.

In the implemented setup, the pulses that exit the stretcher pass through a cylindrical lens telescope to correct for astigmatism incurred from the stretcher. The $\sim$1 nJ, 330 ps seed pulses are then injected into the regenerative amplifier cavity which consists of a plano-concave mirror design with a water-cooled Yb:YAG thin disk, as seen in Figure 2.6. Reflecting off a thin film polarizer (TFP), the S-polarized seed then goes through a Pockels cell (PC) followed by a quarter waveplate

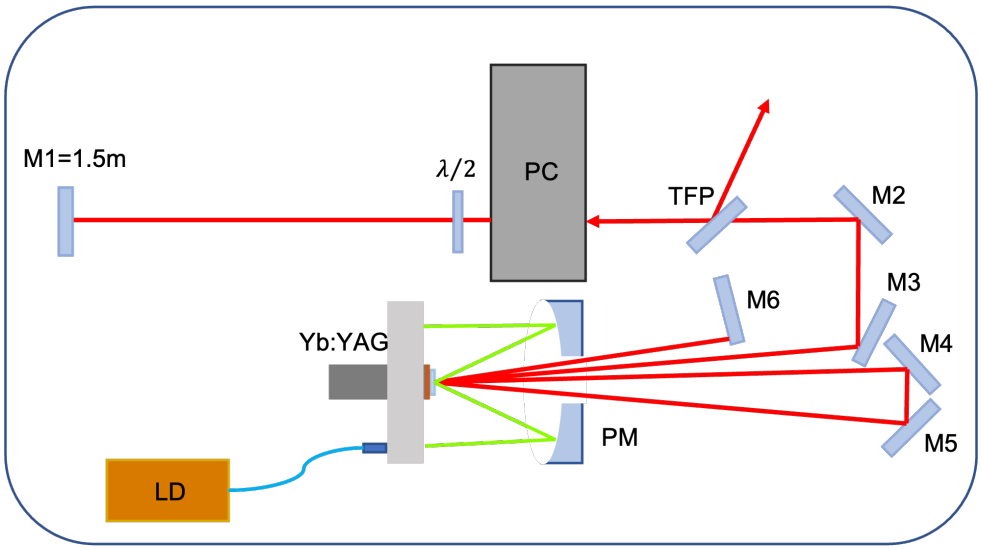

Figure 2.6: Schematic of the room temperature, thin-disk Yb:YAG regenerative amplifier. The cavity is composed of six mirrors (M1-M6), with the Yb:YAG crystal being an active mirror. PC = Pockels cell; $\lambda/2$ = half waveplate; TFP = thin film polarizer; PM = pump mirror, LD = laser diode.

before reflecting off the curved end mirror with f = 1.5 m. By passing through this combination again on the way back towards the TFP, the polarization is changed to P-polarization since the PC voltage is synchronized to be off at the time of seed injection. This polarization rotation couples the seed pulse into the cavity, allowing it to pass through the TFP and on towards the amplifier crystal. The cavity mirrors double pass the seed across the gain crystal until it reaches the second end mirror before following the same path back to the TFP. The pulses oscillate within the regenerative amplifier cavity until gain saturation is achieved.

The gain medium is a Yb:YAG crystal that is 7% doped, 0.5 mm thick, thin disk pumped at the zero-phonon 969 nm line at room temperature by a 200 W fiber coupled laser diode for reduced thermal load, as described in Chapter 1. The crystal is soldered to a copper heatsink which is cooled by water-jet impingement. The pump pulses are 450 μs long at 1 kHz repetition rate and timed to end just before the pulse enters the cavity. The pump is passed eight times across the crystal using a folded mirror setup which results in 95% absorption of the pump power on a 1 mm mode matched spot on the crystal. As with the oscillator, the pump mirror has a hole drilled through the middle to allow the oscillating pulse to travel through it. For each round trip through the cavity, the pulse passes through the active mirror gain medium four times. The pulse is kept

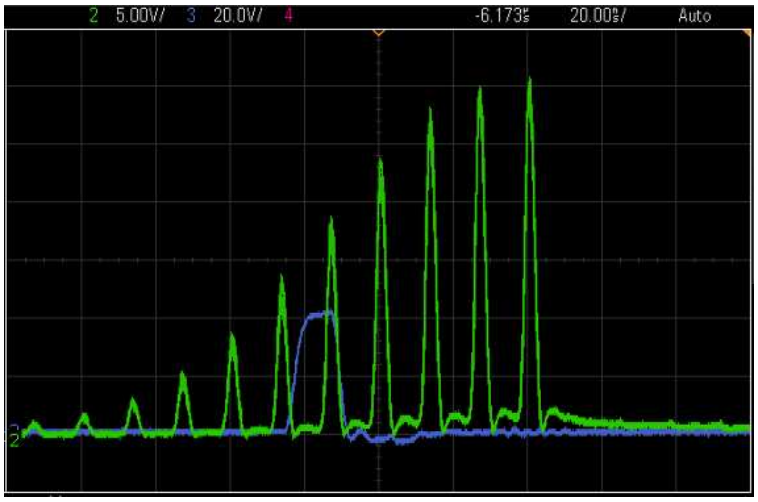

Figure 2.7: Oscilloscope trace of regenerative amplifier output. The green signal is the amplified pulses separated in time according to the cavity length (13.3 ns). The blue signal is the timing window of the cleanup Pockels cell.

within the cavity for the number of passes necessary to reach gain saturation. A small amount of light that leaks from one of the cavity end mirrors is used to monitor the pulse amplification in the cavity, as seen in Figure 2.7. Once the timing of pulse saturation is determined, the Pockels cell is synchronized to eject the pulse before the next pass. Once the pulse is kicked out of the cavity, it is sent through a "cleanup" Pockels cell placed between two cross-polarized calcite crystals. This arrangement improves pulse contrast by chopping off any pre and post pulses from the main pulse as well as preventing feedback from the later amplifier stages. Additionally, the cavity Pockels cell synchronizes pulses to the 1 kHz repetition rate of the system. For any unsynchronized pulses, the cleanup Pockels cell half-wave voltage is zero and they are ejected from the system after a single pass through the cavity. The 1 nJ seed pulses leave the regenerative amplifier with 2 mJ of energy at up to 1 kHz with 0.46 nm of spectral bandwidth retained.

The previous iteration of this system utilized a cryogenically cooled Yb:YAG thin disk regenerative amplifier. This was done in an effort to more closely match the bandwidth and wavelength of the cryogenic power amplifiers that followed the regenerative amplifier stage. However, it was found that the wider bandwidth retained after the room temperature regenerative amplifier was

sufficient to offset the mismatch effects. This also partially mitigates the impact of gain narrowing and thus a shorter transform-limited pulse duration is possible.

2.5 Power Amplifiers and System Performance

Following the laser front end are two cryogenically cooled power amplifiers. Both amplifiers use a multi-pass active mirror geometry for amplification to high pulse energies at 1 kHz. Each amplification stage consists of a cooling head with two Yb:YAG crystals mounted inside a vacuum chamber. Liquid nitrogen flow provides convective cooling across the back surface of each crystal to maximize heat extraction. A fluorescence monitoring system developed in-house allows real time measurement of the crystal temperature at high power [104]. During operation with 1.2 J output at 1 kHZ (1.2 kW average power), the temperature at the center of the pump region was measured to be below 130 K for 1.75 kW average pump power [55].

2.5.1 Yb:YAG Crystal

The Yb:YAG 'thick disk' crystals utilized in these amplifiers are a composite design that is implemented to prevent the effects of amplified spontaneous emission (ASE). One of the drawbacks to cryogenically cooling Yb:YAG is the increased likelihood of parasitic lasing due to the increased emission cross section. This effect reduces the efficiency of the laser by depleting the upper-level population. Crystal designs that suppress ASE are critical for operation at high repetition rates and pulse energies. The crystal in Figure 2.8 is a 40 mm x 40 mm x 5 mm composite design made up of a 2%-at Yb:YAG crystal, a Cr:YAG cladding, and an undoped YAG cap. Both cryogenically cooled power amplifiers in this system use this crystal design.

One method for suppressing ASE is to optically bond an undoped YAG cap to the active surface of the crystal [105, 106]. By bonding a nearly index matched YAG cap to the crystal face, the solid angle for total internal reflection of spontaneously emitted photons is reduced, and the overall structural integrity of the crystal is increased. This undoped cap is also beveled on each side

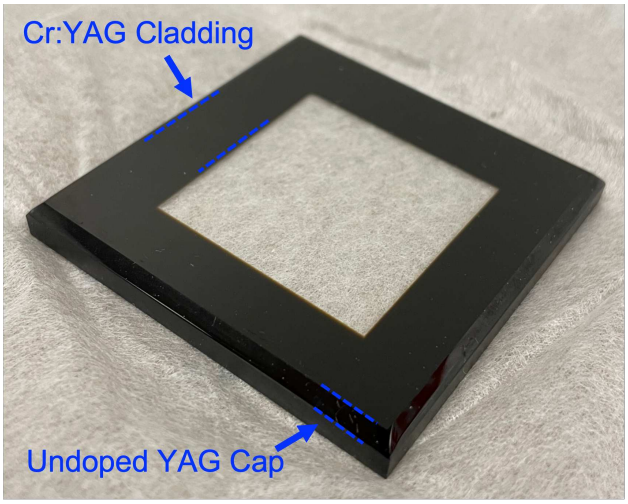

Figure 2.8: Composite Yb:YAG crystal with Cr:YAG cladding and undoped YAG cap anti-ASE features indicated.

to direct any spontaneously emitted photons into the absorbing chromium doped YAG (Cr:YAG) cladding.

The 30 mm x 30 mm x 2 mm active Yb:YAG crystal is bonded on each lateral face with a 35 mm x 10 mm x 2 mm piece of Cr:YAG. The Cr:YAG cladding is used to absorb spontaneously emitted photons. With a measured absorption of 5 cm^{-1} at 1030 nm, the 10 mm width allows for >99% absorption [107]. The outside faces of the Cr:YAG cladding are also given a rough grind to create a nonreflective surface which refracts any ASE photons out of the crystal. These efforts to suppress ASE in this thick crystal design are necessary for efficient operation at high pulse energies.

2.5.2 2nd Stage Amplifier

Prior to entering the 2nd stage, the beam is expanded and collimated with a telescope to a spot size of $\sim$4 mm. This amplifier stage consists of a vacuum chamber housing two Yb:YAG 'thick-disk' crystals, as described above, in a multi-pass active mirror configuration. The crystals are cryogenically cooled by liquid nitrogen in direct contact with the back surface. The previous 500 Hz version of this system had a single crystal 2nd stage setup [49]. The addition of a second crystal helps to distribute the thermal load of the system when operating at high power which improves

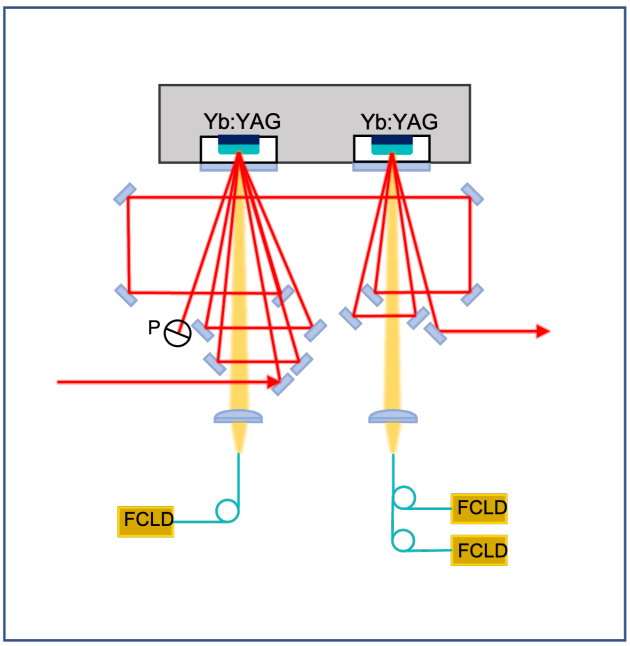

Figure 2.9: Schematic of the 2nd stage Yb:YAG power amplifier. P = periscope; FCLD = fiber coupled laser diode.

the stability and performance of the amplifier. The seed is directed to the first crystal, on the left in Figure 2.9, through an AR940/1030 coated window into the chamber. The Yb:YAG crystal is pumped by a single 400 W fiber-coupled 940 nm laser diode with 450 μs pulses at 1 kHz repetition rate. The pump beam is imaged onto the crystal with an achromatic lens giving a 4 mm spot size for matched overlap with the seed. The multi pass mirror array directs the seed through five passes across the first crystal. A single pass in an active mirror corresponds to traversing the gain material twice, as previously mentioned. After the final pass, a mirror directs the amplified beam to the next crystal. The second crystal is pumped by two 400 W, 940 nm fiber coupled laser diodes which are imaged onto a 4 mm spot like the first crystal. With both crystals, the pump makes a single pass before being directed at a beam dump. The seed makes two additional passes through the second crystal before exiting the amplifier. For the $\sim$1 mJ pulses from the regenerative amplifier, the 2nd stage amplifies up to 100 mJ.

After exiting the 2nd stage, the beam is directed through an 8 mm serrated aperture designed to produce a flat top beam profile for the final stage of amplification, where the uniform profile it creates helps to improve the amplifier efficiency [108]. A CCD camera is set up to collect

the leak through from a mirror after the serrated aperture. This image is used for an automated alignment system which controls mirror actuators for stability during high power operation. After the serrated aperture, the beam is passed through a quarter waveplate and a Faraday isolator which is between two polarizing beam splitters in order to prevent feedback from the final amplifier into the preamplifier.

2.5.3 3rd Stage Amplifier

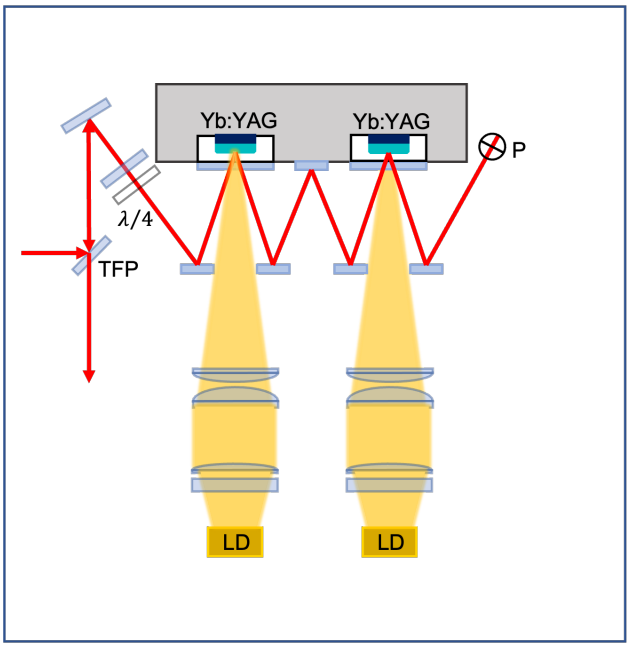

Figure 2.10: Schematic of 3rd stage cryogenic Yb:YAG power amplifier. TFP = thin film polarizer; $\lambda/4$ = quarter wave plate; P = periscope; LD = 6kW laser diodes.

The final stage of amplification in this system endures the highest pump power and greatest thermal load. Before injection into the 3rd stage amplifier, the beam passes through a telescope designed to allow the beam divergence through the final amplifier to be adjusted. This is done for compensation of the thermal lensing effect which occurs at high pump power, as detailed in Chapter 1. Shown in Figure 2.10, a thin film polarizer injects the seed into the multi-pass amplifier which consists of two more of the composite Yb:YAG crystals mounted in a vacuum chamber which facilitates liquid nitrogen cooling of the back surface, similar to the 2nd stage. The crystals are

mounted in custom holders made of alloys with very low thermal expansion coefficients in order to mitigate mechanical stress affecting the beam mode during high power operation. The amplifier head which the liquid nitrogen flows through is made of the same material to help maintain beam mode quality during intense pumping when temperature gradients exist. Unlike the 2nd stage, the 3rd stage amplifier has a symmetric pump and multi pass design for both crystals.

In order to achieve the high pulse energy, both crystals are pumped by 6 kW diode arrays composed of sixty bars that emit 100 W of 940 nm light each. The pump pulse timing is 380 μs at 1 kHz. The divergent output of the diodes requires a series of shaping and imaging optics prior to the crystal. These optics collect, homogenize, and image the pump beam with a flat top profile onto the crystal surface. The pump beam is double passed on each crystal, allowing for greater than 90% absorption of the pump power.

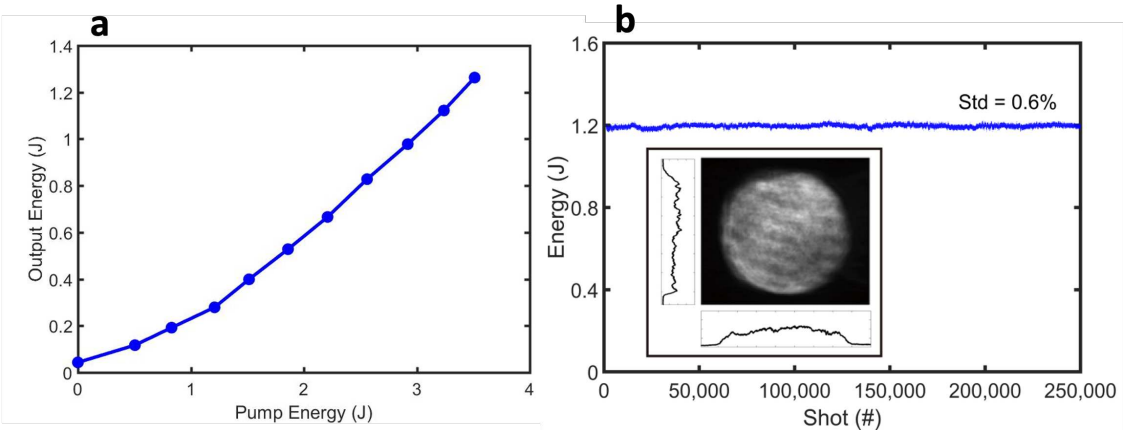

Figure 2.11: Amplifier performance. a) Plot of output energy versus pump energy during 1.2 J operation. b) Recording of 250,000 consecutive shots; the pulse-to-pulse stability has a standard deviation of 0.6%.

This stage is seeded with 70 mJ pulses from the 2nd stage amplifier after passing through a thin film polarizer at the input. The seed then makes two passes across the crystals before being rotated and raised with a periscope to complete two more passes on the crystals. After the fourth pass, the beam passes through a quarter waveplate followed by a zero-degree mirror which sends it back through the quarter waveplate. Now, with the polarization rotated 90 degrees, the beam retraces the original path through the amplifier to complete the final 4 passes before exiting through the

TFP. Figure 2.11 shows the output performance for this final amplifier. A pulse energy of 1.26 J from 3.5 J of pump energy was achieved, giving an optical-to-optical efficiency of ∼36%.

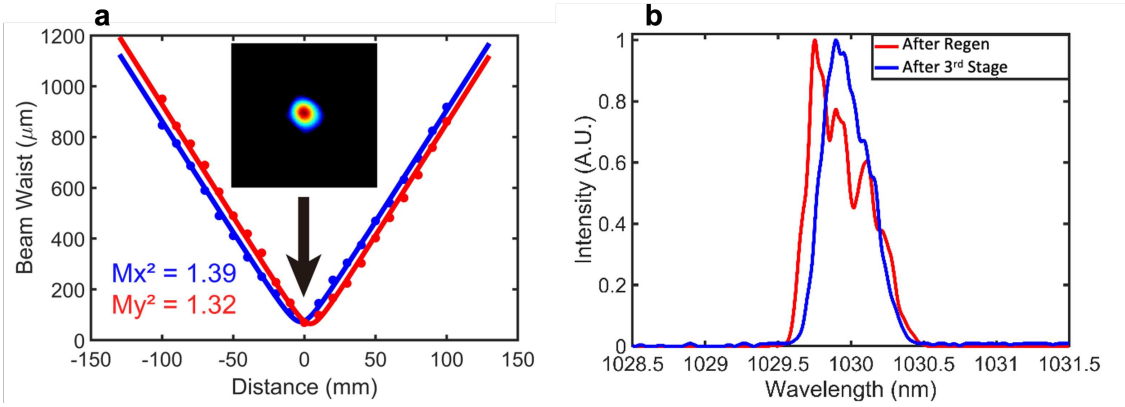

Figure 2.12: Amplified Beam Characterization. a) M^2 measurement of the beam during operation at 1.2 J with M^2 = 1.32 in the horizontal and M^2 = 1.39 in the vertical directions. b) Spectrum after final amplifier stage compared with spectrum after regenerative amplifier stage.

The beam is characterized following the final stage of amplification, prior to injection into the compressor. The far field profile is measured for the beam propagation ratio (M^2) to ensure that mode quality is maintained after amplification to 1.2 J at 1 kHz (Figure 2.12a). Lastly, the spectrum is measured to determine the bandwidth remaining after the two power amplifier stages. As shown in Figure 2.12b, the spectrum at the output of the 3rd stage is centered very close to 1030 nm. The final bandwidth value of 0.35 nm (FWHM) is sufficient to support a transform limited pulse duration of 3.9 ps for a sech^2 pulse shape.

2.6 Pulse Compressor

The amplified pulses exit the 3rd amplification stage through the same thin film polarizer at the input of the amplifier. The output beam is then directed through a telescope to magnify and collimate the beam to a diameter of ∼40 mm before injection into the compressor chamber.

Within the vacuum chamber of the compressor, as shown in Figure 2.13, is a pair of 1740 mm^{-1} dielectric gratings and several HR coated mirrors in a folded layout for directing the beam

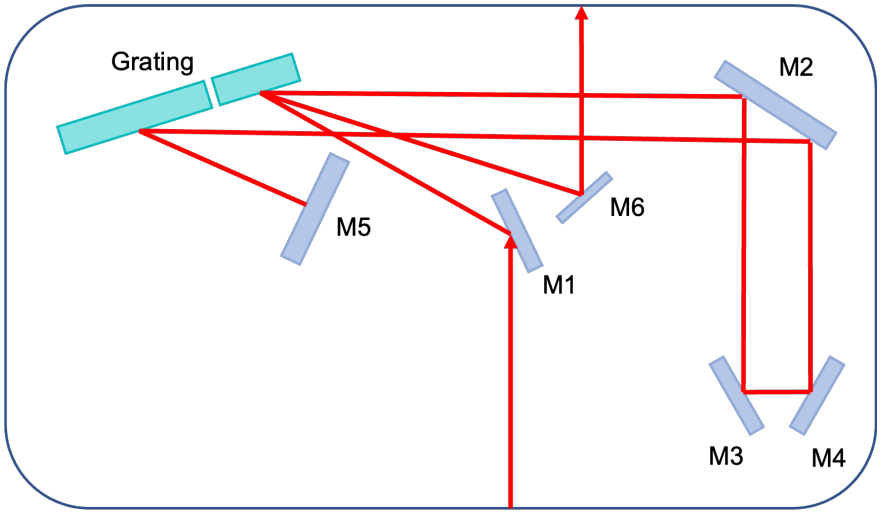

Figure 2.13: Schematic of the grating compressor optical layout. Mirrors (M1-M6) direct the beam through 4 passes across the split grating pair before exiting the chamber.

across the gratings. As with the stretcher, utilizing a folded-mirror setup reduces the footprint of the compressor chamber to just 1 m x 1.6 m while allowing the necessary total path length of 5 m. The pulse enters the chamber through an AR coated window before a mirror (M1) directs it to the grating at an incident angle of 56 degrees. After the first pass on the grating, the pulse travels along the folded mirror setup (M2,M3,M4) before being sent back to the grating for the second pass. At this point, the pulse refracts off the grating to a roof mirror (M5) setup which changes the beam height in order to send it back for a third and fourth pass on the gratings. Following the final pass on the grating, the compressed pulse is ejected from the chamber by an output mirror (M6).

As mentioned in the last section, slight gain narrowing in the final amplifier reduces the bandwidth of the spectrum from 0.46 nm after the regenerative amplifier to 0.35 nm (FWHM). The compressor is designed to remove the positive dispersion of the stretcher by creating an equivalent amount of negative dispersion. As a result, the compressor design effectively matches that of the stretcher: with the grating separation L = 2.5 m, grating line density d = 1740 mm^{-1}, and incident angle of θ_i = 56 degrees. The absence of the Martinez-style telescope (or spherical concave mirror in the case of the stretcher in this system) allows the compressor gratings to produce negative dispersion, as Treacy first described [14]. The negative GDD of the compressor can be calculated, as

with the stretcher, from Equation (2.1):

$$\frac{d^2\varphi}{d\omega^2} = -\frac{N\lambda^3 L}{2\pi c^2 d^2}\left[1-\left(\frac{\lambda}{d}-sin\theta\right)^2\right]^{-\frac{3}{2}} \tag{2.5}$$

This gives a second order dispersion value of:

$$GDD \approx -1.51 \times 10^9\ fs^2 \tag{2.6}$$

which is, by design, the 'normal' equivalent to the 'anomalous' dispersion of the stretcher. With 0.35 nm bandwidth after the 3rd amplification stage, the transform-limited pulse duration is 3.9 ps (sech^2). Following this dispersion compensation, the pulsewidth of the output pulses are measured to be 4.48 ps, as seen in the autocorrelation result shown in Figure 2.14. The compression efficiency achieved with this grating compressor design is $\sim$90%.

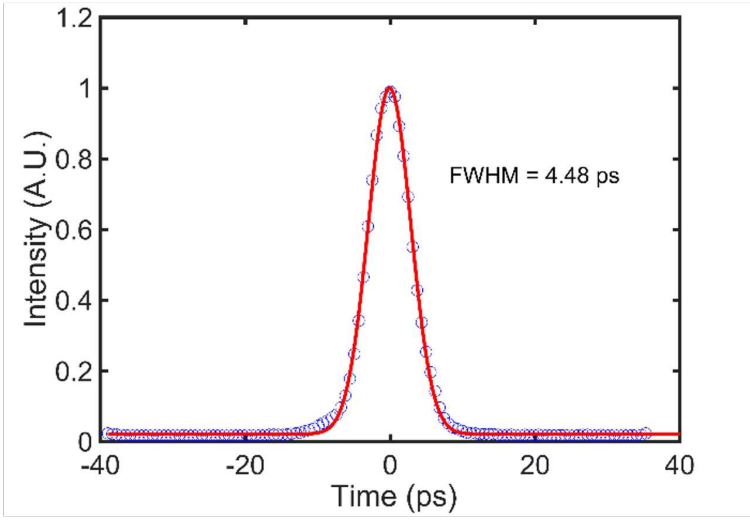

Figure 2.14: SHG autocorrelation measurement for the compressed output during 1.1 kW, 1 kHz, operation showing 4.48 ps pulse duration.

2.7 Summary and Applications

In summary, the diode-pumped laser system has achieved >1 J pulses at 1 kHz repetition rate for an average power in excess of 1 kW. This average power is a world record for Joule-level, picosecond pulses, at 1 kHz repetition rate. As mentioned previously, this level of performance has enabled applications including soft x-ray generation, second harmonic pumping, and filament-guided discharges in air. The results of a filament-guided discharge experiment utilizing the laser system detailed in this chapter are described in the next chapter.

Chapter 3

Picosecond Laser Filament Guiding of Electrical Discharges in Air at 1 kHz Repetition Rate

3.1 Introduction

The propagation of high-power laser pulses in air has been studied since the early years of laser development, motivated by potential applications. Laser pulses of sufficient intensity lead to ionization of air molecules and plasma formation. Beginning in the 1970s, the prospect that this interaction could be used to trigger and guide electrical discharges, such as lightning, was experimentally studied with some success [109–111]. Further investigation using long pulse, high energy lasers produced high-voltage discharges guided across meter scale gaps [86,87,112]. These studies were limited to nanosecond pulse durations, which resulted in the formation of a discontinuous chain of conductive plasma balls. The long pulse duration causes avalanche ionization at the leading edge of the pulse which produces a dense plasma that is optically opaque to the trailing edge, limiting pulse propagation [77]. While guiding was possible due to the conductive plasma balls promoting leader formation [87], the limited pulse propagation distance and high pulse energy required made these systems poorly suited for guiding discharges over long distances. The development of ultrashort pulse lasers, aided by chirped pulse amplification [10] renewed the interest in this area of research due to their high intensity capabilities. For a laser pulse of power greater than the critical power for self-focusing, atmospheric propagation becomes heavily affected by nonlinear responses, resulting in a self-sustaining channeling known as filamentation. Discovered by Braun et al. (1995) [79], filamentation is primarily due to a dynamic balance between self-focusing via the optical Kerr effect and plasma defocusing. For femtosecond pulses the result is typically a narrow (of the order of 100 μm), weakly ionized plasma channel of uniform density

which is capable of propagating hundreds of meters with plasma lifetimes of the order of several nanoseconds, as detailed in [80, 81].

Following this discovery, the continuous plasma channel produced by femtosecond filamentation was seen as an effective way to trigger and guide electrical discharges. As with natural lightning, electric discharges in the laboratory are typically initiated through a highly conductive 'leader' which propagates by the formation of 'streamers' at its head. For an atmospheric discharge at STP, the critical field for spontaneous breakdown is $\sim$30 kV/cm. Several experiments were successful in initiating and guiding the discharge process, an effect that was associated with the filament formed plasma facilitating leader growth between electrodes [89, 113]. However, other experiments have shown that discharges triggered and guided by filamentation can also occur in the absence of streamers [90], including those triggered with laser pulses of > 2 ps duration [91]. Due to the relatively low electron density [114] of the filaments generated by mJ-level femtosecond pulses, the generated plasma is weakly conductive [115] and has a short (ns) lifetime, making it poorly suited for sustaining discharges. The hydrodynamic response of the air following filament formation was identified as a key mechanism for triggering and guiding discharges [92]. Using time-resolved interferometry [93, 116] and diffractometry [117], a low-density channel of similar geometry to the filament was found in the wake of the ultrafast filamentary pulses. This hydrodynamic response of the air is caused by the deposition of laser energy which heats the air along the channel, leading to a pressure wave that expands radially, leaving behind an underdense region at the center [92, 93, 116–118]. When aligned between electrodes, this localized depression in air density along the filament path acts as a channel which, in accordance with the Paschen curve [119], enables discharges to be triggered by an applied electric field which is below the threshold for breakdown in air.

Most laser-guided discharge experiments have been conducted at low (f = 10 Hz) repetition rates with femtosecond lasers [90, 120–125]. In particular, Ti:Sa based systems have been utilized due to their capability of producing femtosecond filamentation with low pulse energy, and their widespread commercial availability. Since the molecular density hole has been shown to decay by

thermal diffusion on a millisecond timescale [93], at such low repetition rates the time between laser pulses allows for complete relaxation of the surrounding air before the next pulse arrives. The more recent development of kHz-level laser systems capable of generating the high intensity necessary for filamentation has enabled the study in a new regime in which the medium does not completely recover before the arrival of the next discharge-inducing laser pulse. A few experiments have been conducted with femtosecond Ti:Sa lasers operating at 1 kHZ repetition rate [96, 126, 127]. They showed the formation of a long lived quasi-permanent density depression [126] of greater magnitude than observed at low repetition rates [96]. This cumulative effect was recently studied in work that also reports a reduction in breakdown voltage compared with low rep rate discharges when voltage is applied by triggering a spark-gap prior to the arrival of a laser pulse [96].

Figure 3.1: Filament-guided lightning. Photograph taken from the recent publication on the first successfully guided lightning discharge utilizing filamentation from a high repetition rate Yb:YAG infrared laser [54]. (From [128])

Recently, diode-pumped Yb:YAG-based IR lasers producing high power picosecond pulses at repetition rates up to 1 kHz have become available [35, 55, 129] for filamentation and discharge guiding research [94, 95, 97]. The short time between shots at high repetition rates (1 ms at 1 kHz) allows a given laser pulse to interact with the air perturbation caused by the preceding pulses [94, 95, 97]. Filament lengths up to 70 m have been recently reported with 720 mJ laser energies and pulse durations of 0.92 ps at 1 kHz repetition rate [54]. Studies on the effects of longer pulse durations suggest that a hotter, denser plasma is created compared with fs pulses, which could aid in discharge formation [95, 130]. Results of breakdown voltage for single shot near-infrared laser pulses of up to 10 J energy and durations between 0.7 and 10 ps found a further 30% reduction for the longer pulses [91]. In an experiment with a 1030 nm laser generating 0.9 ps pulses with 150 mJ of pulse energy at 1 kHz repetition rate, a reduction in breakdown voltage by a factor of more than 2 X was reported [94]. Another study with 1030 nm, 1.5 ps pulses of 100 mJ energy found a factor of 3 X reduction in breakdown voltage when the repetition rate was increased from 10 Hz to 1 kHz [95]. This breakdown voltage reduction was attributed to the cumulative effect of the hydrodynamic response of the air around the filament at high repetition rates.

Here we examine discharges guided by the filamentation of high-energy picosecond pulses of 7 ps duration and up to 250 mJ energy from a λ = 1030 nm wavelength laser operating at repetition rates up to 1 kHz. We successfully demonstrate the generation of consistent and stable discharge columns at 1 kHz repetition rate. A breakdown voltage reduction of up to 4.2 X is observed to result dominantly from the perturbation caused by a single laser pulse, with the cumulative effects playing only a secondary role. Similar breakdown voltage reductions are observed at both 100 Hz and 1 kHz repetition rates. A current proportional to the laser pulse energy arises as soon as the laser pulse arrives, initiating a high impedance discharge. Full breakdown, characterized by impedance collapse and the onset of high current conduction, occurs 100s of ns to a few μs later, following the formation of concentrated conducting channels in the gaps that link the filamentary plasma channel and the electrodes.

3.2 Experimental Setup and Methodology

This filament-guided discharge experiment was performed using the λ_L = 1.03 μm Yb:YAG laser system detailed in Chapter 2. This all diode-pumped, cryogenically cooled CPA laser system was configured for this experiment to provide laser pulses of 7 ps duration with pulse energies up to 250 mJ at repetition rates up to 1 kHz [55]. A schematic of the experimental setup is shown in Fig. 3.2c.

Following the compressor stage of the system, a 3 cm diameter S-polarized beam is focused onto a ∼70 μm (FWHM) diameter spot using a 2.2 m focal length lens. The repetition rate (f) of the laser pulses was varied between f = 0.01 to 1 kHz by adjusting the Pockels cell after the regenerative amplifier. The laser pulse energy (E_L) was varied in the range E_L = 10 – 200 mJ by selecting the seed pulse energy injected into the 3rd stage power amplifier. This allowed the 3rd stage pump pulse energy to be maintained constant to avoid significant variation in the thermal lens. The initial electrode setup for the experiment incorporated two brass balls of 2 cm diameter with 3.8 mm holes drilled through the centers. However, it was found that the guiding of discharges over long gaps was affected by the nonuniform electric field around the balls. To increase field uniformity, two parallel circular brass plates with rounded edges and face diameters of 13 cm were used, as seen in Figure 3.2a. The laser beam passes through 3.8 mm diameter holes drilled on axis through the electrodes. A translation stage was set up such that the separation of the two plates could be varied in the range L = 2 cm to 10 cm. A 1.7 nF ceramic capacitor, charged through a resistor, was directly connected to the anode electrode and the cathode was grounded. The capacitor was charged using either a current supply (Glassman PS/LT015P132) or a voltage supply (Hypotronics 8100-10), operable at voltages up to either 15 kV or 70 kV, respectively. The current supply is more highly filtered, offering a more stable source for repetition-rated discharges, while the higher voltage power supply was used for larger electrode separation measurements. The charging resistor was selected to be either R_c = 280 kΩ or R_c = 175 MΩ. The lower value was used for faster charging of the capacitor with the voltage supply for high repetition rate measurements, such that the capacitor is nearly fully charged when the next laser pulse arrives. The higher resistor

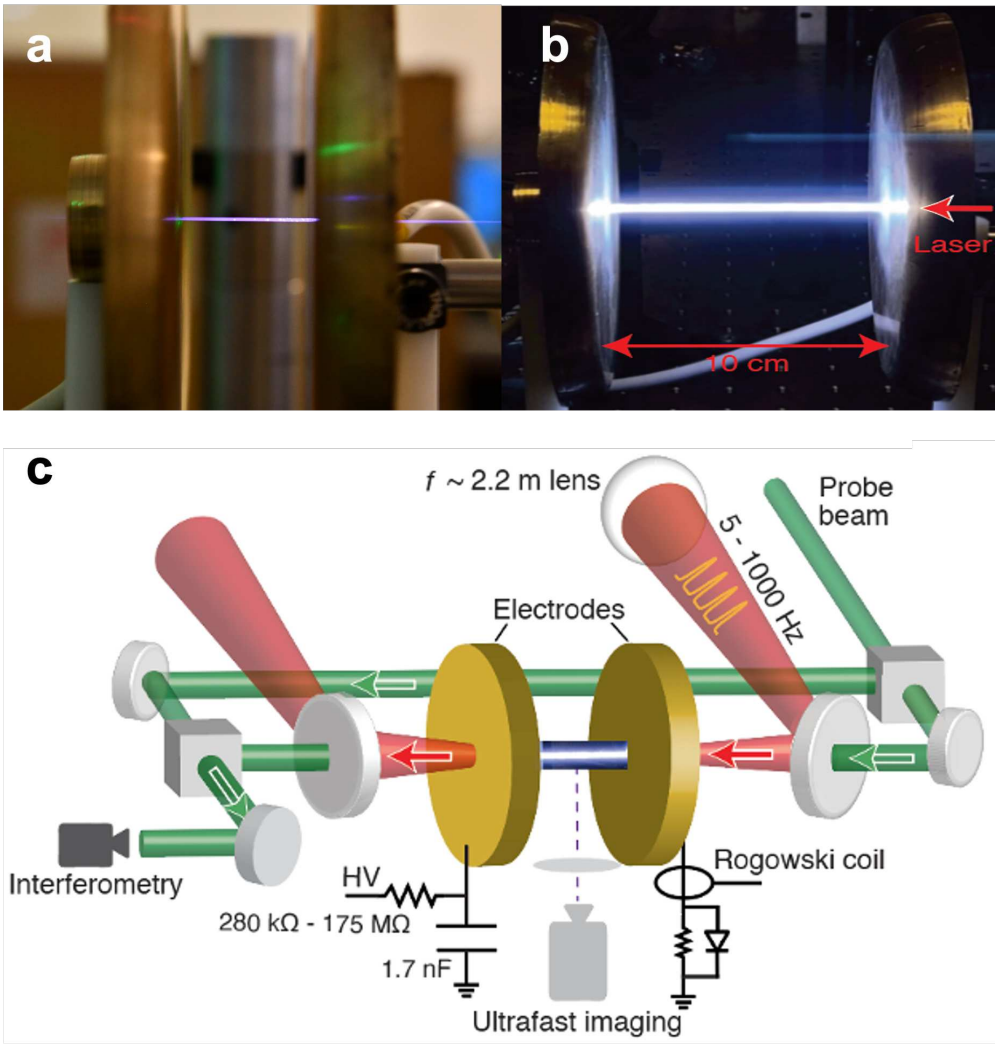

Figure 3.2: (a) Photograph of filament fluorescence for laser pulse energy of 200 mJ, repetition rate 1 kHz and plate separation of 4 cm. (b) Photograph integrated over 17 discharge events, taken with a 60 frames per second camera, for a laser pulse energy of 200 mJ, repetition rate 1 kHz and plate separation of 10 cm. (c) Schematic of the experimental setup: Probe beam shown in longitudinal configuration. The charging resistance (R_c) is varied in the range R_c = 280 kΩ – 175 MΩ. The power supply (HV) is either a voltage or current supply, detailed in the main text. The current pulse is monitored with a Rogowski coil across the ground loop.

value was used for breakdown measurements in which the train of laser pulses repetitively samples the gap for breakdown as the voltage is slowly increased. Figure 3.2a displays a photograph of a laser filament between the brass electrodes, and Fig. 3.2b shows a corresponding laser-guided discharge channel 10 cm in length. The image is integrated over 17 discharge events at 1 kHz repetition rate, showing the consistency of the guided discharges that were generated.

A number of optical and electrical diagnostics were implemented. The electrical diagnostics consisted of a high voltage probe (Tektronix P6015A) for measuring the breakdown voltage, and a magnetic probe to measure the current pulse. The voltage drop across a resistor placed in the ground electrode connection was measured with a differential probe to also provide a measurement of the current. Photodiodes were used to measure the times of arrival of the laser and probe pulses with respect to the discharge event. These diagnostics were coupled to a deep memory scope (LeCroy Wavepro 7300A), capable of saving traces up to seconds duration with 10 ns temporal resolution. The optical diagnostics included imaging systems for measuring the discharge-generated light and allowed for either time-integrated or time-resolved image sequences to be recorded. The latter made use of a fast micro-channel plate intensified framing camera (Invisible Vision Ultra UHSi-12) capable of recording sequences of up to 12 frames of variable temporal separation with a minimum exposure window of 5 ns. The sequential gating capability with this resolution allowed the early formation of the discharge to be characterized by recording sequences of images of the discharge channel fluorescence. Additionally, Mach Zehnder interferometers using a second harmonic green probe beam (λ_P = 532 nm) were deployed in two different angular configurations: longitudinal along the discharge axis (case illustrated in Fig. 3.2c) or transverse, at either grazing incidence (11.5 degrees) or normal incidence, to probe the discharge channel evolution. Time resolved interferograms were recorded using either the gating provided by the second harmonic probe laser pulse ($\sim$5 ns resolution) and a standard CCD camera (Basler acA1920-25um), or by using the high-speed framing camera (5 ns image resolution).

3.3 Results and Discussion

3.3.1 Discharges at 1 kHz

The influence of laser pulse parameters on the filamentation and discharge processes were characterized in order to derive a physical understanding. For high repetition rate discharges, a characteristic of interest is the probability of discharge occurrence. In previous experiments, efforts were made to increase this probability.

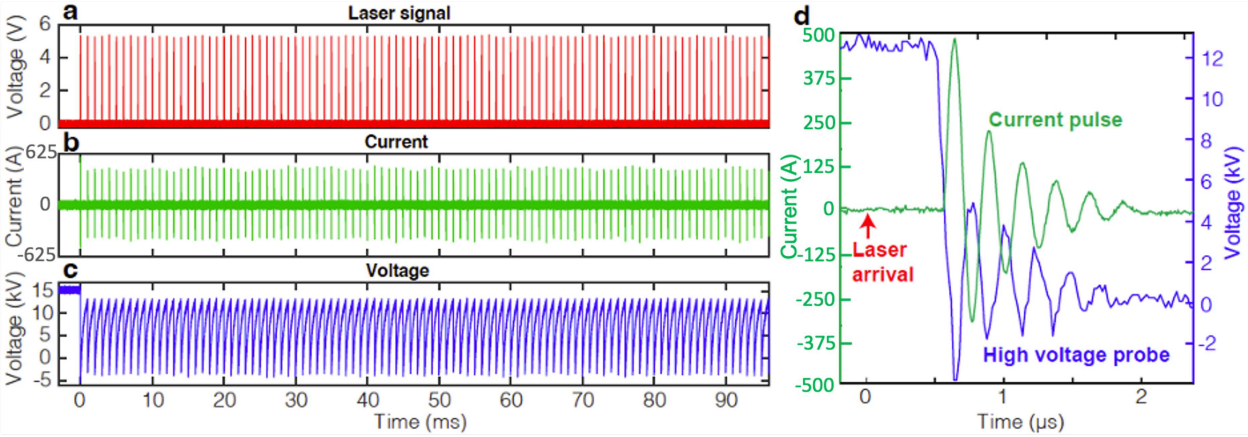

Figure 3.3: (a-c) Electrical measurements (labelled) of a laser guided discharge, operating at a repetition rate f = 1.0 kHz, E_L = 150 mJ laser energy and L = 2 cm electrode separation. A sequence of approximately 100 laser-triggered discharges are shown. (d) Example of single discharge event.

Figure 3.3 shows an example of discharge pulse electrical data for a train of laser filament guided discharges at 1 kHz repetition rate in which 100% of the pulses induce breakdown. The frames (a-c) show the laser pulse time-of-arrival measured with a photodiode, the current pulse, and the voltage drop across the electrode gap, respectively, for ∼100 consecutive discharges. These measurements were taken for an electrode gap of 2 cm and with laser pulse energy of E_L = 150 mJ. The voltage of the current supply was set to 15 kV to charge the capacitor with a charging time constant τ = 0.5 ms. At 1 kHz the time interval separating each laser pulse is 1 ms, meaning that at the time the subsequent laser pulse arrives the capacitor is charged to ∼85% of its maximum voltage. This charging rate is sufficient to consistently cause a discharge event upon the arrival of each laser pulse. Notice that the current of the initial discharge of the sequence, which corresponds

to having the capacitor fully charged and suddenly unblocking the laser beam, is larger due to the larger initial overvoltage with respect to the breakdown voltage. Figure 3.3(b) shows that each subsequent laser pulse is responsible for causing a breakdown event with reproducible current pulses. The average power dumped into the discharge is ∼440 W. Figure 3.3(d) displays a zoomed-in example image of the current and voltage measurements for a single discharge event. In this case the current is under damped and the time of laser pulse arrival is indicated.

3.3.2 Breakdown voltage thresholds

At the fundamental level, the action of the laser filament is twofold: it reduces the breakdown voltage (V_b) required to initiate a discharge event, and provides a straight channel for guiding the current between electrodes. For this experiment, it was important to characterize the breakdown voltage, V_b, as a function of laser pulse energy (E_L), discharge gap (L), and repetition rate (f). To accomplish this, the capacitor was charged slowly with the R_c = 175 MΩ (corresponding to τ = 300 ms) resistor and the laser pulses were left unblocked while operating at varied repetition rates up to 1 kHz. In this way, the high repetition rate train of pulses samples the gap with continuously increasing voltage until breakdown is achieved, determining the threshold value. Figure 3.4(a-d) displays V_b as a function of laser pulse energy E_L, for four electrode separation distances, L = (2, 4, 8, 10 cm), and two different repetition rates, f = 100 Hz and 1 kHz. In order to supply a sufficiently high voltage to achieve breakdown in the longest gaps, the voltage supply was used instead of the current supply due to it's 15 kV limit. The value of the breakdown voltage in the absence of a laser pulse is indicated in black for each gap (a-d). Beyond an electrode separation of 2 cm the self-breakdown voltage (without a laser pulse) exceeds the capabilities of our voltage supply; the calculated values for these gaps are indicated instead.

From Chapter 1, the critical power required for self-focusing, resulting in filamentation, for the λ = 1030 nm laser used in this experiment is 5.3 GW. When operating with 7 ps pulses, this critical power corresponds to a pulse energy of 37 mJ. As such, a sharp drop in V_b is measured as the laser

pulse energy E_L is increased from E_L = 0 mJ to 50 mJ (see Fig. 3.4(a-d)). Notably, the effects of increasing E_L become less pronounced for E_L > 50 mJ, with V_b eventually reaching a plateau.

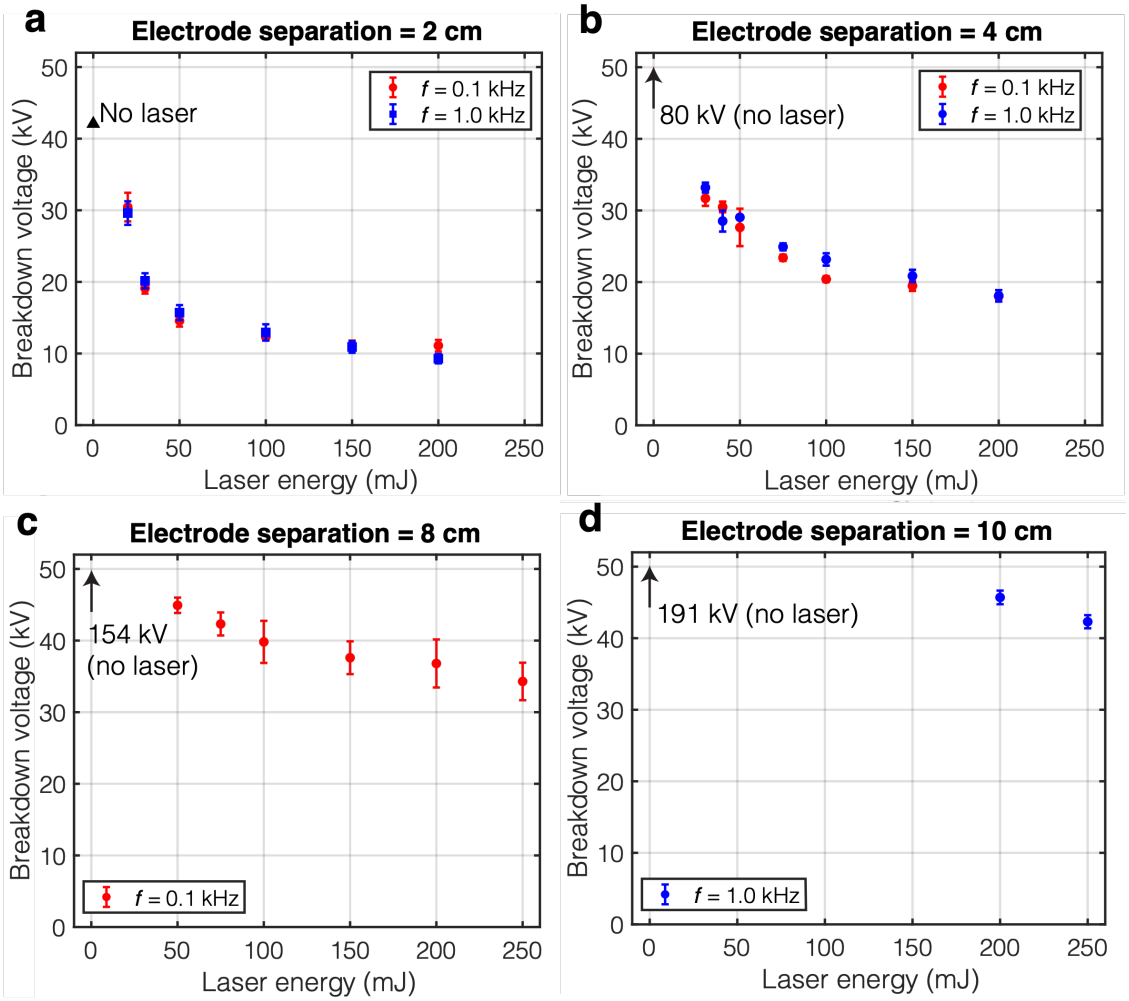

Figure 3.4: (a-d) Breakdown voltage (V_b) as a function of laser pulse energy (E_L), for two laser pulse repetition rates (f) and electrode separations. (a) L = 2 cm; (b) L = 4 cm; (c) L = 8 cm and (d) L = 10 cm. The breakdown voltage without a laser pulse present (details described in main text) is indicated in black at the E_L = 0 mJ position.

3.3.3 Discharge delay time

In this section, further characterization of the filament-guided discharge process is shown with measurements of the delay time between arrival of the laser pulse and the onset of a discharge. Figure 3.5(a,b) shows the discharge delay time as a function of applied voltage for different laser pulse energies. This data was collected for an electrode separation of 2 cm at 5 Hz repetition rate. The low repetition rate was chosen to ensure sufficient time between pulses such that the process of unblocking the laser didn't interfere with the measurement. The delay time for each of the three laser pulse energies (E_L = 40, 100, 200 mJ) is first measured near the threshold breakdown voltage value under these conditions. At these lower voltages, discharges are less consistent and result in longer delay times with larger variation in delay times from shot to shot. When the supply voltage is increased, the percentage of consistent discharges also increases and the delay times become shorter with less variation between shots. Initially, this trend is also true for increasing laser pulse energy. However, for voltages larger than 25 kV, there is no further decrease in delay when the energy is increased above 100 mJ, as shown in Figure 3.5(a,b). These results show that for a pulse energy of 100 mJ, the breakdown delay decreases from 1 μs when 15 kV is applied, to <40 ns when 40 kV is applied, a factor of >25x.

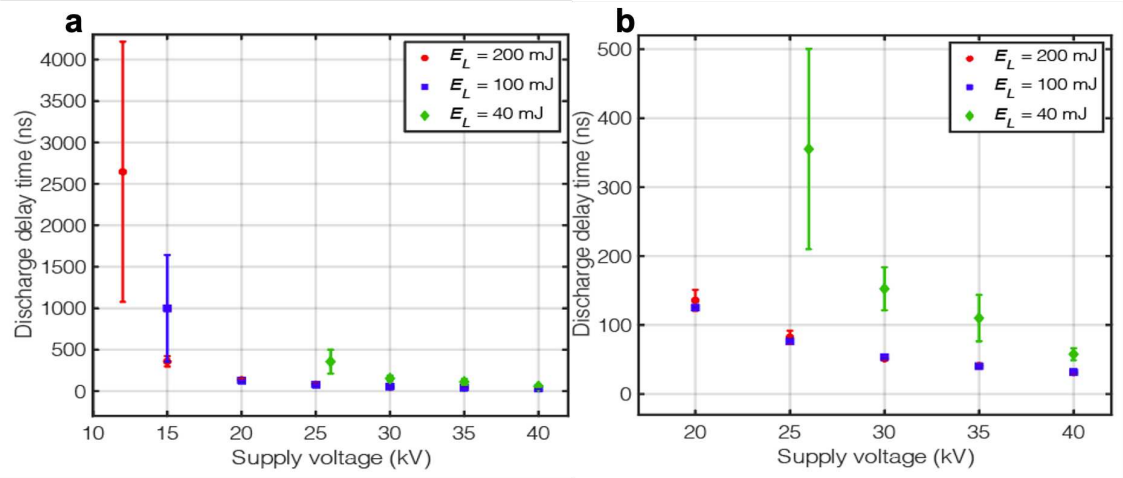

Figure 3.5: Discharge breakdown delay as a function of applied voltage for discharges initiated by laser pulses with three different energies. The electrode gap was 2 cm and the repetition rate was 5 Hz. A zoomed in view of the data in a) for delays less than 500 ns is illustrated in b) for better visualization. For voltages above 25 kV no difference in breakdown delay is observed for laser pulse energies greater than 100 mJ.

3.3.4 Breakdown voltage reduction

The role of the laser created filament in reducing the breakdown voltage necessary for discharge has been discussed. From this experiment, Figure 3.6(a,b) shows that for E_L = 200 mJ the breakdown voltage is reduced by a factor between 4 and 4.2 X over the entire range of electrode separations investigated when compared to the breakdown voltage in the absence of a laser. For breakdown without the laser, $V_b(E_L = 0mJ)$ was measured for a range of small electrode separations L = (0.5, 1, 1.5 and 2 cm), and is shown in Figure 3.6(a,b) to have the expected linear dependence as a function of inter-electrode distance.

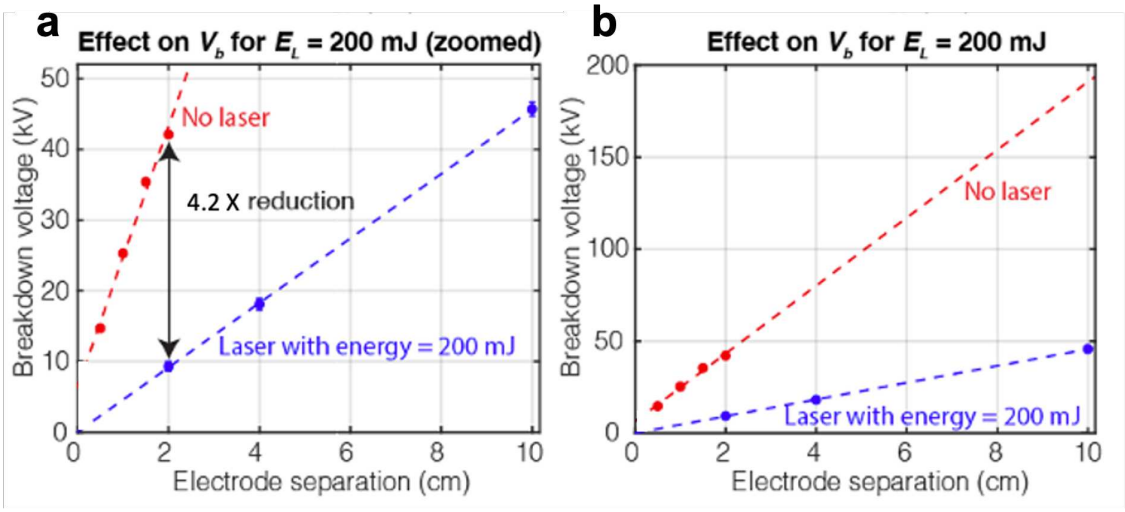

Figure 3.6: (a,b) V_b as a function of L, for E_L = 200 mJ alongside the no laser case. (a) Zoomed in view of the breakdown voltages up to 50 kV to highlight the reduction between the two cases; (b) displays the full voltage axis. The dashed lines correspond to a linear fit to the data points. An extrapolation is shown for distances L larger than 2 cm.

Previous studies of laser filaments generated at high repetition rate have observed the generation of a permanent density depression resulting from the cumulative effect of multiple laser shots before full relaxation of the medium can occur [94–96, 126]. A previous laser filament formation experiment conducted at 1 kHz repetition rate employing the same laser and setup utilized in this experiment measured a density depression of $\sim$20% at the time of arrival of a laser pulse, caused by the previous pulses in the pulse train [97]. The existence of this permanent density depression

was confirmed by longitudinal interferometry comparing the channel at 100 Hz and 1 kHz, as shown in Figure 3.7.

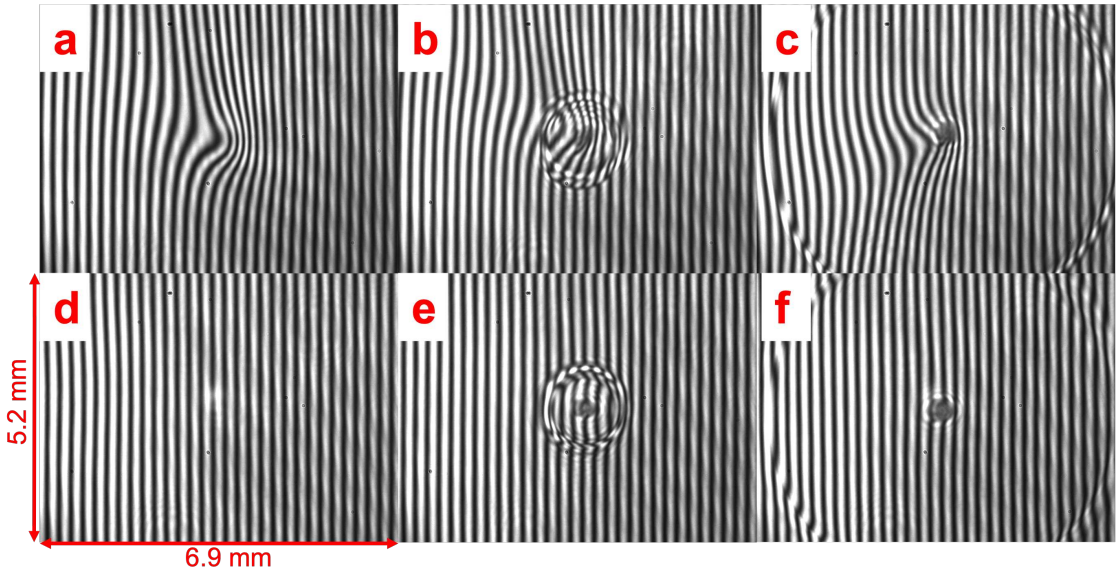

Figure 3.7: Permanent density depression at high repetition rate. Longitudinal interferograms (L x H: 6.9 x 5.2 mm) for $E_L = 150mJ$ at (a-c) f = 1 kHz and (d-f) f = 100 Hz. A noticeable perturbation is present 10 μs prior to arrival of the laser pulse at 1 kHz (a), and is shown to persist through the 2 μs (b) and 10 μs (c) frames taken after the laser pulse. No such perturbation is seen in the frames taken at 100 Hz (d-f).

However, while this persistent depression will lower the breakdown voltage, it cannot account for the large reduction of up to 4.2 X measured in this experiment. We have observed that the reduction in breakdown voltage from a single laser pulse far exceeds the value that can be attributed to the permanent density depression resulting from high repetition rate. This result, as shown below, indicates that the cumulative effect at high repetition rate plays only a minor role in reducing V_b by the large factors measured in this experiment. The breakdown voltage dependence on gas density has been thoroughly studied for spark gap switches [131, 132]. For this experiment, where large plane electrodes were utilized to improve uniformity of the electric field, the relationship between air density and breakdown electric field is well described by:

$$E(kV/cm) = 24.5P(atm) + 6.7\sqrt{P(atm)/L(cm)} \tag{3.1}$$

where E is the breakdown electric field, P is pressure and L is electrode plate separation. Here the pressure is assumed at constant temperature and is therefore proportional to the gas density. The ambient air pressure at altitude in Fort Collins, CO (>5000 ft) is $\sim$0.833 atm, giving a breakdown electric field of 26.5 kV/cm. The 20% density depression due to the cumulative effect at high repetition rates lowers the breakdown electric field by a factor of 1.2 X to $E = 21.8kV/cm$. By contrast, a factor of more than 4 X reduction in V_b is measured in this experiment (Fig. 3.6a). This result indicates that the combination of the density depression and conductive plasma channel caused by a single laser pulse is dominant in decreasing the breakdown voltage. Further supporting this conclusion are the measurements in Fig 3.3 (a,b) which show that the breakdown voltage for 100 Hz and 1 kHz filament-guided discharges at different electrode separations were practically equivalent.

Analysis of transverse interferograms taken at different delay times with respect to laser pulse arrival further corroborate the dominant effect of a single pulse by. In Figure 3.8(a), a transverse interferogram (L x H: 1.2 x 2 mm) taken 300 ns after arrival of the laser pulse is shown with a well defined central depression and radially expanding shockwave. A phase map generated from the fringe pattern shows the well-defined boundaries of the central density depression and the early stage of the radially expanding shockwave (Figure 3.8b). Figure 3.8(c) shows the radial profile of the central density depression in terms of phase shift (blue and black lines) and air density (red line). The air density profile was computed assuming similar symmetry. This result shows that 300 ns after arrival of the laser pulse, a density depression of 75% relative to the ambient air density is created. This central depression has a diameter of $\sim$300 μm. The spike in density beyond the level of ambient air ($\sim$2.2 x 10^{19} cm^{-3}) denotes the shockwave. This reduction in air density by $\sim$75% for a single pulse far exceeds the cumulative depression at high repetition rates and forms the main contribution to the large reduction in breakdown voltage measured here.

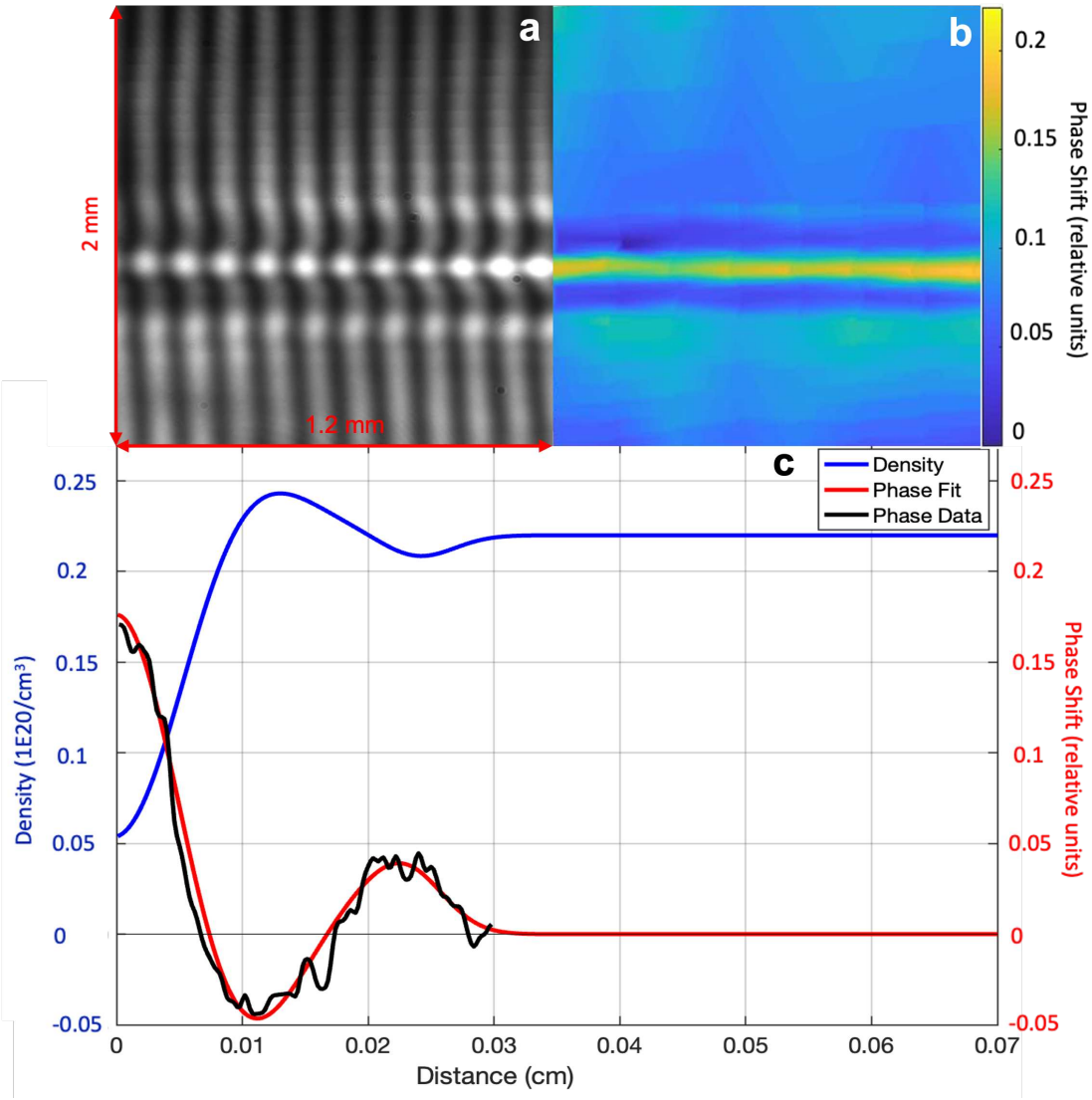

Figure 3.8: Radial density profile 300 ns after the arrival of the laser pulse. (a) Transverse interferogram (L X H: 1.2 x 2 mm) showing the central density depression and radially expanding shockwave. (b) Phase shift map of the transverse interferogram showing the boundaries of the central depression and expanding shockwave. (c) Radial profile of extracted phase shift (black, relative units), phase data fit (red, relative units), and air density (blue, 1E20/cm^3).

3.3.5 Initial current flow and breakdown

The process of full breakdown is complex and comprises several phases. Prior to the arrival of a laser pulse, an electric field is established between the plate electrodes. The intense laser pulse causes optical field ionization to occur, with subsequent avalanche ionization dominating in the case of 7 ps laser pulse duration utilized in this experiment [97]. Upon stripping electrons from the air molecules, a filamentary plasma channel is created which extends beyond the length of the gap between electrodes. Laser heating produces a radially expanding shockwave and creates an axial density depression.

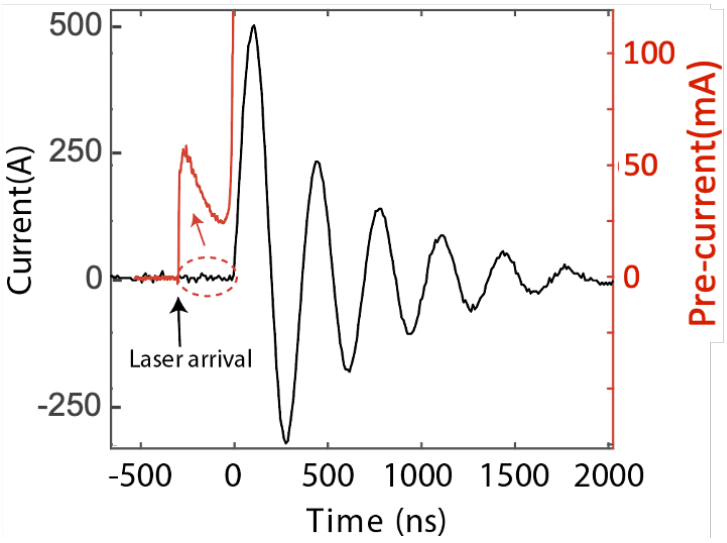

Figure 3.9: Current evolution illustrating the pre-breakdown current (red), magnified relative to the full breakdown current pulse (black), initiated with a 140 mJ laser pulse in a 2 cm discharge gap biased at 15 kV.

Current flow, typically on the order of several 10s to 100s of mA, is observed to occur immediately following the arrival of the laser pulse, as shown in Figure 3.9. This 'precurrent' corresponds to a high impedance phase of the discharge, prior to the time of full breakdown which is characterized by the collapse of the impedance. The onset of this precurrent is characterized by a rapid rise that is likely a result of re-arrangement of charges generated by the laser pulse in the applied electric field. Following this initial rise is a sustained current of magnitude and temporal evolution

dependent on the laser pulse energy and applied electric field. In cases of high overvoltage, where the applied voltage significantly exceeds the threshold voltage for breakdown, precurrent values as high as a few hundred mA have been measured. The lifetime of the precurrent phase, which occurs with the onset of breakdown, depends on the applied electric field and can range from hundreds of nanoseconds to multiple microseconds.

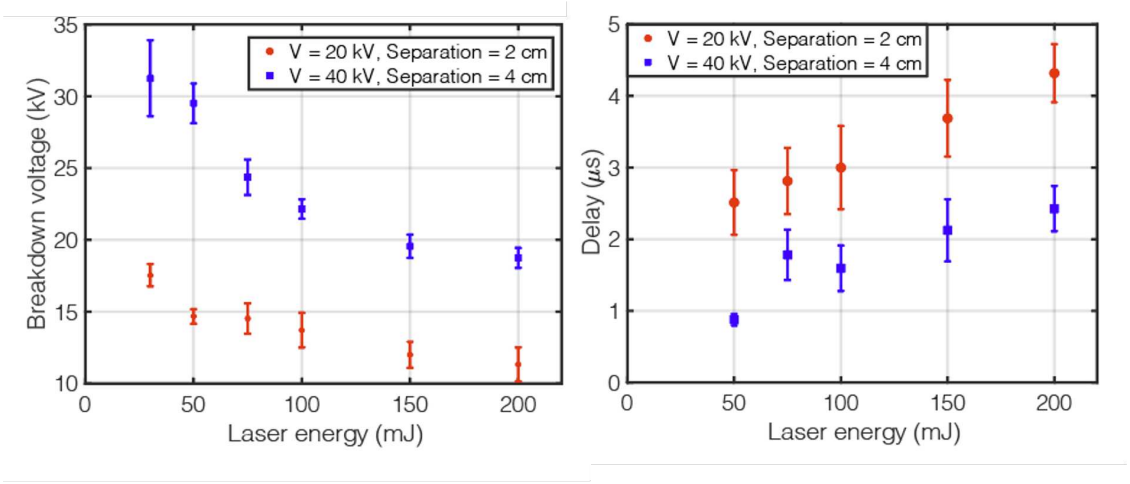

Figure 3.10: Constant E/N: Breakdown voltage (a), and breakdown delay with respect to the arrival of the laser pulse as a function of laser pulse energy (b) for 2 cm and 4 cm electrode separation. The voltage applied was adjusted to have initially equal E/N values.

The typical value of the impedance in the pre-breakdown phase ranges from 0.1 MΩ to a few MΩ, depending on laser pulse energy and the voltage applied. The impedance is the sum of resistance of the filamentary plasma column that is located on the axis of the holes through the electrodes, plus the resistance of the air gaps between the column and the electrodes. The non-negligible role of these gaps becomes evident by conducting measurements of discharges with similar ratios of electric field to molecular density (E/N), a major scaling parameter in electrical discharges. For this purpose, measurements were conducted for discharges across 2 cm and 4 cm electrode separations, applying twice the voltage in the 4 cm case. The measured breakdown voltage was found to nearly double in the case of the longer channel, as shown in Fig. 3.10(a). However, the time delay between the arrival of the laser pulse and the breakdown is measured to significantly decrease in the case of the 4 cm discharge relative to the 2 cm (Fig. 3.10b). This can

be ascribed to the fact that in this case the gaps between the filament-initiated plasma column and the electrodes are subject to twice the electric field. This indicates that the role of these small gaps (< 1.9 mm between the filament channel and the electrode) in the breakdown cannot be neglected.

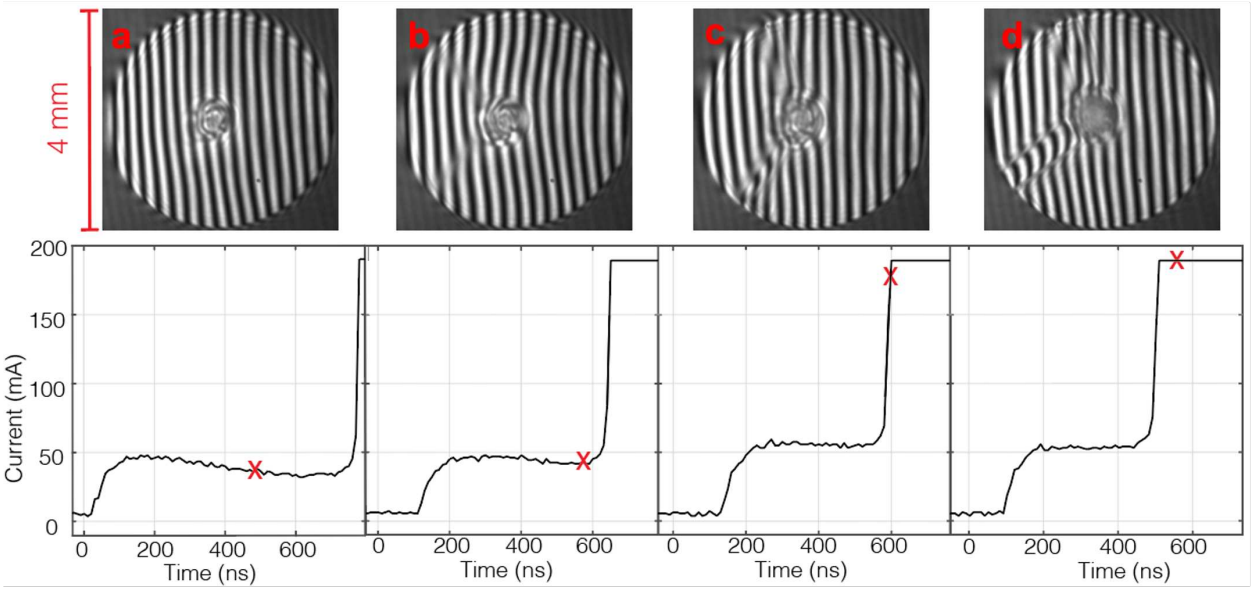

Figure 3.11: (a-d) On-axis interferograms showing the development of plasma channels linking the laser filament-initiated plasma column to the hollowed electrodes, with corresponding current pulses below indicating the time at which the image was taken (red x). The data was collected for an electrode separation of 2 cm, and laser pulse energy of 150 mJ. The circular region containing the fringes is the electrode hole, with a diameter of 3.8 mm.

Figure 3.11 shows on-axis interferograms taken at different times following arrival of the laser pulse and their corresponding positions in time relative to the evolution of the current preceding and following breakdown. These images give important insight into the transition from the high impedance, precurrent phase to the high current phase following impedance collapse and breakdown. At the earliest time, (a), there is no visible connection between the filament and the surrounding electrode hole which would allow current to flow. During this time, current may be conducted from the electrode to the filament channel by a high impedance, spatially distributed, glow-type discharge. It is known that glow discharges can occur in air at atmospheric pressure, with several studies conducted [133, 134]. The regions near the electrodes in glow discharges are locations of high electric field within which instabilities can lead to the glow discharge plasma

collapsing into an arc [134]. This glow-to-arc transition is accompanied by a collapse of the impedance. The subsequent times, Fig. 3.11(b-d), reveal the formation of concentrated discharge channels (arcs) bridging the gap between the electrodes and the filament discharge channel. Figure 3.11(b) shows an example of the earliest time that these conducting channels appear, typically several hundred nanoseconds after the laser pulse arrives. Once these radially conductive channels form across the gap, breakdown occurs with the collapse of the impedance and the rapid discharge of the capacitor. Notice in Figure 3.11(c,d) that the gap arcs expand as the rapid current increase heats them by Joule heating.

3.3.6 Streamerless discharge formation

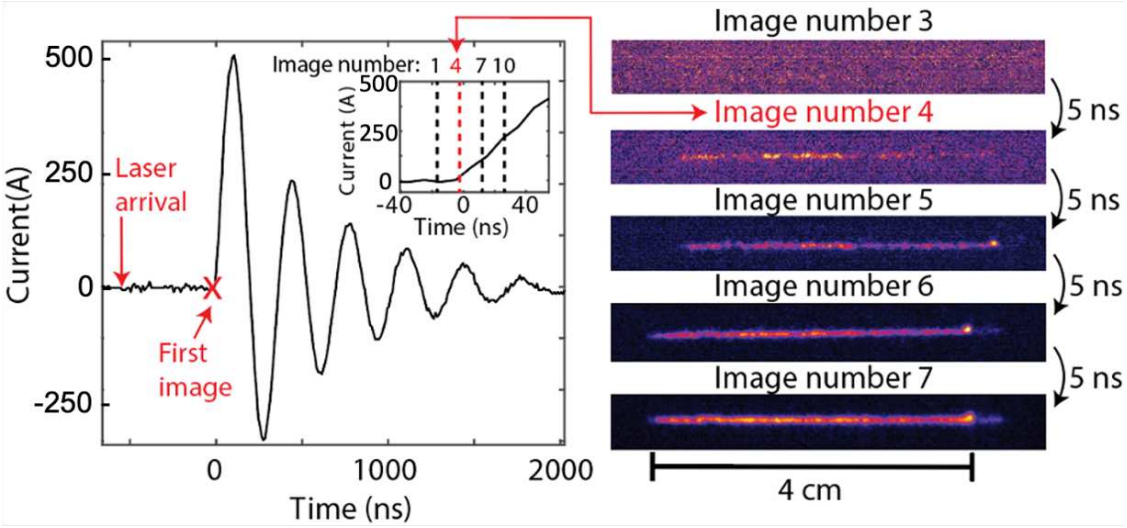

Figure 3.12: Streamerless discharge formation. Sequence of images of the plasma column near the time of breakdown taken 5 ns apart with the ultrafast gating camera. The time of each image with respect to the current pulse is indicated.

The evolution of the plasma column after the time of breakdown leading to the rapid rise of the current was observed using fast sequential imaging with a temporal resolution of 5 ns. Figure 3.12 shows the first five frames of a sequence of 12 contiguous images spanning the evolution of the discharge during the first 60 ns after breakdown for an electrode gap of 4 cm. Prior to breakdown, no light is detected by the micro-channel plate (MCP) intensified camera. Plasma

light emission, initially detected in the first 5 ns frame after breakdown, is observed to be uniform across the entire gap and to grow in intensity on every frame as the current increases. No evidence of streamers propagating across the electrode gap is detected. For a velocity of 1 x 10^8 cm/s, which is on the high end of the typical velocity for streamers [85, 135, 136], it would take 40 ns for a streamer to bridge the electrode gap, a sufficiently long time for the framing camera to detect it. Interferograms acquired at different times during the low current phase preceding breakdown also show a lack of streamer formation. Rather, a uniform channel bridges the electrode separation gap as filament charge created by the laser pulse flows uniformly across the gap. As mentioned before, this streamerless discharge formation for laser filament-guided discharges has been previously reported [90], in particular for laser pulses of picosecond duration [91].

3.4 Conclusions

We have initiated and guided electrical discharges in atmospheric air at repetition rates of up to 1 kHz with laser filaments generated by λ = 1030 nm picosecond pulses of up to 250 mJ energy. In these multi-ps pulse generated plasma channels, ionization is initiated by photoionization and is dominated by collisional avalanche. The laser-created filament is measured to reduce the discharge breakdown voltage by a factor of up to 4.2 X, which to our knowledge is the largest reported for a discharge between dc biased electrodes. The laser pulse arrival and filament formation is observed to cause the immediate onset of current flow between the biased electrodes, the magnitude of which is proportional to the laser pulse energy. This current that precedes the full breakdown is typically of the order of several tens of milliamps, and the impedance of the discharge at this time is between 0.1 MΩ to a few MΩ. The gaps between the filament and the discharge electrodes are observed to play a significant role in the breakdown. Axial interferograms taken at this pre-breakdown time show the absence of concentrated current flow between the filament and the electrodes. This suggests that during this phase the current across these gaps is conducted by a diffused high impedance glow discharge. Full breakdown, characterized by collapse of the impedance and a rapid order of magnitude increase of the current, is observed to be preceded by the formation of localized current channels linking the filament to the electrodes. Full breakdown occurs a few hundred ns to a few μs after the arrival of the laser pulse, depending on the laser pulse energy and voltage applied. The results indicate that the gaps between the filament and the electrodes cannot be neglected in analyzing the dynamics of table-top filament discharge experiments. The breakdown voltages for discharges initiated by laser filaments generated at 100 Hz and 1 kHz was measured to be practically the same. This is consistent with the results of transverse interferometry which shows that the filament formed by a single laser pulse causes a density depression that can reach 75%, compared with the relatively small (eg. 20%) permanent depression resulting from the cumulative effect at high repetition rates. From the point of view of applications, the results obtained demonstrate the stable repetitive generation of discharge channels in the atmosphere at 1 kHz repetition rate. The

increased understanding of the physics of the formation of laser filament-guided discharges in air at kHz repetition rate can be expected to contribute their use in applications.

Chapter 4

Summary

The work presented in this thesis was made possible by the development of a diode pumped cryogenically cooled picosecond Yb:YAG CPA laser system at the Advanced Beam Laboratory at Colorado State University. This diode pumped CPA laser system takes advantage of the superior properties of cryogenically cooled Yb:YAG as gain material to generate high pulse energy pulses at repetition rates up to 1 kHz. Stretched seed pulses are amplified to the Joule level in an amplifier chain consisting of a regenerative amplifier followed by two cryogenically cooled power amplifiers. The Yb:YAG power amplifiers use a thick-disk crystal geometry designed to minimize amplified spontaneous emission while also considering thermal effects at high repetition rate, high power operation. Following the final stage of amplification, the pulses are compressed by a dielectric grating compressor which imparts a negative chirp to counter the positive dispersion of the stretched pulses. The robust design of this system generates pulses of up to 1.1 J and 4.5 ps duration at 1 kHz repetition rate, corresponding to an average power of 1.1 kW, a record for energy for picosecond lasers operating at 1 kHz.

The performance of this laser system makes it possible to research filamentation, a type of collimated nonlinear pulse propagation wherein Kerr self-focusing is balanced with plasma refractive defocusing, at kHz repetition rate. This self-channeling propagation regime is capable of persisting for distances of hundreds of meters. Applications of filamentation include remote sensing, weather control, and laser-guided electrical discharges. The study of the filament-guided electrical discharges generated at high repetition rate is the main subject of this thesis. The physics of filament guided discharges initiated by high energy (up to 200 mJ) 1030 nm ultrafast (7 ps) laser pulses at repetition rates up to 1 kHz across electrode gaps up to 10 cm was explored in depth. The experimental results were obtained through a number of diagnostics. The use of a high voltage and a magnetic probe allowed measurement of the breakdown voltage and current pulse respectively. The output of these probes, in addition to a photodiode signal for timing of pulse/probe beam ar-

rival with respect to a discharge, were monitored on a high-resolution oscilloscope. Finally, both longitudinal and transverse interferometers enabled characterization of the discharge channel evolution via time-resolved interferograms. Additionally, a high-speed framing camera allowed for visual characterization of discharge formation on both long and short timescales.

Plasma interferometry shows that at 1 kHz repetition rate the relaxation time of the medium is longer than the time delay between pulses. This leads to a cumulative air density depression that can be expected to lower the breakdown voltage, though it is shown that for the conditions investigated here this effect is secondary to single pulse effects in lowering the breakdown voltage. For discharges triggered by 200mJ laser pulses, a reduction of the breakdown voltage by 4.2 X was measured, which to our knowledge is the largest discharge threshold lowering reported for filament-initiated discharges with DC biased electrodes. The breakdown voltages measured at 100 Hz and 1 kHz repetition rates are nearly the same. This is consistent with the fact that interferometry shows that the filament formed by a single laser shot causes a deep density depression that can reach 75%, compared with the 20% density depression that is measured 10 μs prior to the arrival of a laser pulse in a sustained 1 kHz sequence.

The laser pulse arrival and filament formation are observed to cause the immediate onset of current flow between the biased electrodes, the magnitude of which is proportional to the laser pulse energy. This current that precedes the full breakdown is typically of the order of several tens of milliamps depending on the voltage applied. The impedance of the discharge at this time ranges from 0.1 MΩ to a few MΩ. The gaps between the filament and the discharge electrodes are observed to play a significant role in the breakdown. Axial interferograms taken at this pre-breakdown time do not observe any evidence of concentrated current flow between the filament and the electrodes. This suggests that during this phase the current across these gaps is conducted by a diffused glow that subsequently collapses into an arc, followed by full breakdown characterized by a collapse of the impedance and a rapid orders of magnitude increase of the current. Full breakdown is measured to occur a few hundred ns to a few μs after the arrival of the laser pulse, depending on the laser pulse energy and voltage applied. As the current increases the diameter of

these channels rapidly grows. The electrode spacing is also shown to play a role in the breakdown delay. When the applied electric field is kept constant, minimum delay is achieved for the longest discharge channels. This again is indicative of the significant role played in the breakdown by the gaps between the filament and the electrodes.

These results contribute to the physical understanding of laser-filament guided discharges generated at high repetition rates, which is of interest for applications.

Bibliography

[1] TH Maiman. Stimulated optical radiation in ruby. *Nature*, 187(4736):493–494, 1960.

[2] FJ McClung and RW Hellwarth. Giant optical pulsations from ruby. *Applied Optics*, 1(101):103–105, 1962.

[3] Willis E Lamb Jr. Theory of an optical maser. *Physical Review*, 134(6A):A1429, 1964.

[4] LE Hargrove, Richard L Fork, and MA Pollack. Locking of he–ne laser modes induced by synchronous intracavity modulation. *Applied Physics Letters*, 5(1):4–5, 1964.

[5] Herman A Haus. Mode-locking of lasers. *IEEE Journal of Selected Topics in Quantum Electronics*, 6(6):1173–1185, 2000.

[6] K Thyagarajan and Ajoy Ghatak. *Lasers: fundamentals and applications*. Springer Science & Business Media, 2010.

[7] Walter Koechner. *Solid-state laser engineering*, volume 1. Springer, 2013.

[8] David E Spence, P Np Kean, and Wilson Sibbett. 60-fsec pulse generation from a self-mode-locked ti: sapphire laser. *Optics letters*, 16(1):42–44, 1991.

[9] Ferenc Krausz, Martin E Fermann, Thomas Brabec, Peter F Curley, Martin Hofer, Manfred H Ober, Christian Spielmann, Ernst Wintner, and AJ Schmidt. Femtosecond solid-state lasers. *IEEE Journal of Quantum Electronics*, 28(10):2097–2122, 1992.

[10] Donna Strickland and Gerard Mourou. Compression of amplified chirped optical pulses. *Optics communications*, 55(6):447–449, 1985.

[11] Rajeev Khare and Paritosh K Shukla. Temporal stretching of laser pulses. *Coherence and ultrashort pulse laser emission*, pages 206–207, 2010.

[12] Turan Erdogan. Dispersion and pulses. https://www.plymouthgrating.com/guidance/technical-notes/fundamentals/dispersion-and-pulses/, 2018.

[13] Sterling Backus, Charles G Durfee III, Margaret M Murnane, and Henry C Kapteyn. High power ultrafast lasers. *Review of scientific instruments*, 69(3):1207–1223, 1998.

[14] Edmond Treacy. Optical pulse compression with diffraction gratings. *IEEE Journal of quantum Electronics*, 5(9):454–458, 1969.

[15] Oscar E Martinez. Grating and prism compressors in the case of finite beam size. *JOSA B*, 3(7):929–934, 1986.

[16] Roger Newman. Excitation of the nd3+ fluorescence in cawo4 by recombination radiation in gaas. *Journal of Applied Physics*, 34(2):437–437, 1963.

[17] Monte Ross. Yag laser operation by semiconductor laser pumping. *Proceedings of the IEEE*, 56(2):196–197, 1968.

[18] T.Y. Fan. Diode pumped solid state lasers. *The Lincoln Lab Journal*, 3(3):413–425, 1990.

[19] Paul Crump, Jun Wang, Trevor Crum, Suhit Das, Mark DeVito, Weimin Dong, Jason Farmer, Yan Feng, Mike Grimshaw, Damian Wise, et al. > 360 w and> 70% efficient gaas-based diode lasers. In *High-Power Diode Laser Technology and Applications III*, volume 5711, pages 21–29. SPIE, 2005.

[20] LF Johnson, JE Geusic, and LG Van Uitert. Coherent oscillations from tm3+, ho3+, yb3+ and er3+ ions in yttrium aluminum garnet. *Applied Physics Letters*, 7(5):127–129, 1965.

[21] J Ronald Thornton, William D Fountain, Graham W Flint, and Thomas G Crow. Properties of neodymium laser materials. *Applied Optics*, 8(6):1087–1102, 1969.

[22] JE Geusic, HM Marcos, and LeGrand Van Uitert. Laser oscillations in nd-doped yttrium aluminum, yttrium gallium and gadolinium garnets. *Applied Physics Letters*, 4(10):182–184, 1964.

[23] Sébastien Chénais, Frédéric Druon, Sébastien Forget, François Balembois, and Patrick Georges. On thermal effects in solid-state lasers: The case of ytterbium-doped materials. *Progress in quantum electronics*, 30(4):89–153, 2006.

[24] Guenter Huber, Christian Kränkel, and Klaus Petermann. Solid-state lasers: status and future. *JOSA B*, 27(11):B93–B105, 2010.

[25] David C Brown, Sten Tornegård, and Joseph Kolis. Cryogenic nanosecond and picosecond high average and peak power (happ) pump lasers for ultrafast applications. *High Power Laser Science and Engineering*, 4, 2016.

[26] Yuan Sui, Mingheng Yuan, Zhenao Bai, and Zhongwei Fan. Recent development of high-energy short-pulse lasers with cryogenically cooled yb: Yag. *Applied Sciences*, 12(8):3711, 2022.

[27] Jun Dong, Michael Bass, Yanli Mao, Peizhen Deng, and Fuxi Gan. Dependence of the yb 3+ emission cross section and lifetime on temperature and concentration in yttrium aluminum garnet. *JOSA B*, 20(9):1975–1979, 2003.

[28] David C Brown, Rufus L Cone, Yongchen Sun, and Randy W Equall. Yb: Yag absorption at ambient and cryogenic temperatures. *IEEE Journal of selected topics in quantum electronics*, 11(3):604–612, 2005.

[29] RL Aggarwal, DJ Ripin, JR Ochoa, and TY Fan. Measurement of thermo-optic properties of Y3AL5O12, LU3AL5O12, YAIO3, LIYF4, LILUF4, BAY2F8, KGD(WO4)2, and KY(WO4)2 laser crystals in the 80–300 k temperature range. *Journal of Applied Physics*, 98(10):103514, 2005.

[30] Glen A Slack, DW Oliver, RM Chrenko, and S Roberts. Optical absorption of y 3 al 5 o 12 from 10-to 55 000-cm- 1 wave numbers. *Physical review*, 177(3):1308, 1969.

[31] Rosalind Wynne, John L Daneu, and Tso Yee Fan. Thermal coefficients of the expansion and refractive index in yag. *Applied optics*, 38(15):3282–3284, 1999.

[32] Glen A Slack and DW Oliver. Thermal conductivity of garnets and phonon scattering by rare-earth ions. *Physical Review B*, 4(2):592, 1971.

[33] Junji Kawanaka, Koichi Yamakawa, Hajime Nishioka, and Ken-ichi Ueda. 30-mj, diode-pumped, chirped-pulse yb: Ylf regenerative amplifier. *Optics letters*, 28(21):2121–2123, 2003.

[34] J Tümmler, R Jung, H Stiel, PV Nickles, and W Sandner. High-repetition-rate chirped-pulse-amplification thin-disk laser system with joule-level pulse energy. *Optics letters*, 34(9):1378–1380, 2009.

[35] Thomas Metzger, Alexander Schwarz, Catherine Yuriko Teisset, Dirk Sutter, Alexander Killi, Reinhard Kienberger, and Ferenc Krausz. High-repetition-rate picosecond pump laser based on a yb: Yag disk amplifier for optical parametric amplification. *Optics letters*, 34(14):2123–2125, 2009.

[36] Federico J Furch, Brendan A Reagan, Bradley M Luther, Alden H Curtis, Shaun P Meehan, and Jorge J Rocca. Demonstration of an all-diode-pumped soft x-ray laser. *Optics letters*, 34(21):3352–3354, 2009.

[37] Kyung-Han Hong, Juliet T Gopinath, Darren Rand, Aleem M Siddiqui, Shu-Wei Huang, Enbang Li, Benjamin J Eggleton, John D Hybl, Tso Yee Fan, and Franz X Kärtner. High-energy, khz-repetition-rate, ps cryogenic yb: Yag chirped-pulse amplifier. *Optics letters*, 35(11):1752–1754, 2010.

[38] Darren A Rand, Scot EJ Shaw, Juan R Ochoa, Daniel J Ripin, Andrew Taylor, Tso Yee Fan, Hector Martin, Scott Hawes, Jim Zhang, Samvel Sarkisyan, et al. Picosecond pulses from a cryogenically cooled, composite amplifier using yb: Yag and yb: Gsag. *Optics letters*, 36(3):340–342, 2011.

[39] Sandro Klingebiel, Christoph Wandt, Christoph Skrobol, Izhar Ahmad, Sergei A Trushin, Zsuzsanna Major, Ferenc Krausz, and Stefan Karsch. High energy picosecond yb: Yag cpa

system at 10 hz repetition rate for pumping optical parametric amplifiers. *Optics Express*, 19(6):5357–5363, 2011.

[40] AH Curtis, BA Reagan, KA Wernsing, FJ Furch, BM Luther, and JJ Rocca. Demonstration of a compact 100 hz, 0.1 j, diode-pumped picosecond laser. *Optics letters*, 36(11):2164–2166, 2011.

[41] Daniel E Miller, Luis E Zapata, Daniel J Ripin, and Tso Yee Fan. Sub-picosecond pulses at 100 w average power from a yb: Ylf chirped-pulse amplification system. *Optics letters*, 37(13):2700–2702, 2012.

[42] Brendan A Reagan, Cory Bamgarten, Keith Wernsing, Herman Bravo, Mark Woolston, Alden Curtis, Federico J Furch, Bradley M Luther, Dinesh Patel, Carmen S Menoni, et al. 1 joule, 100 hz repetition rate, picosecond cpa laser for driving high average power soft x-ray lasers. In *CLEO: Science and Innovations*, pages SM1F–4. Optica Publishing Group, 2014.

[43] Luis E Zapata, Hua Lin, Anne-Laure Calendron, Huseyin Cankaya, Michael Hemmer, Fabian Reichert, W Ronny Huang, Eduardo Granados, Kyung-Han Hong, and Franz X Kärtner. Cryogenic yb: Yag composite-thin-disk for high energy and average power amplifiers. *Optics letters*, 40(11):2610–2613, 2015.

[44] Chun-Lin Chang, Peter Krogen, Kyung-Han Hong, Luis E Zapata, Jeffrey Moses, Anne-Laure Calendron, Houkun Liang, Chien-Jen Lai, Gregory J Stein, Phillip D Keathley, et al. High-energy, khz, picosecond hybrid yb-doped chirped-pulse amplifier. *Optics express*, 23(8):10132–10144, 2015.

[45] Robert Jung, Johannes Tümmler, Thomas Nubbemeyer, and Ingo Will. Thin-disk ring amplifier for high pulse energy. *Optics express*, 24(5):4375–4381, 2016.

[46] Hanieh Fattahi, Ayman Alismail, Haochuan Wang, Jonathan Brons, Oleg Pronin, Theresa Buberl, Lénárd Vámos, Gunnar Arisholm, Abdallah M Azzeer, and Ferenc Krausz. High-

power, 1-ps, all-yb: Yag thin-disk regenerative amplifier. *Optics letters*, 41(6):1126–1129, 2016.

[47] Jakub Novák, Jonathan T Green, Thomas Metzger, Tomáš Mazanec, Bedřich Himmel, Martin Horáček, Zbyněk Hubka, Robert Boge, Roman Antipenkov, František Batysta, et al. Thin disk amplifier-based 40 mj, 1 khz, picosecond laser at 515 nm. *Optics express*, 24(6):5728–5733, 2016.

[48] Jonathan Fischer, Alexander-Cornelius Heinrich, Simon Maier, Julian Jungwirth, Daniele Brida, and Alfred Leitenstorfer. 615 fs pulses with 17 mj energy generated by an yb: thin-disk amplifier at 3 khz repetition rate. *Optics Letters*, 41(2):246–249, 2016.

[49] Cory Baumgarten, Michael Pedicone, Herman Bravo, Hanchen Wang, Liang Yin, Carmen S Menoni, Jorge J Rocca, and Brendan A Reagan. 1 j, 0.5 khz repetition rate picosecond laser. *Optics Letters*, 41(14):3339–3342, 2016.

[50] Thomas Nubbemeyer, Martin Kaumanns, Moritz Ueffing, Martin Gorjan, Ayman Alismail, Hanieh Fattahi, Jonathan Brons, Oleg Pronin, Helena G Barros, Zsuzsanna Major, et al. 1 kw, 200 mj picosecond thin-disk laser system. *Optics letters*, 42(7):1381–1384, 2017.

[51] FX Morrissey, TY Fan, DE Miller, and D Rand. Picosecond kilohertz-class cryogenically cooled multistage yb-doped chirped pulse amplifier. *Optics Letters*, 42(4):707–710, 2017.

[52] Bruno E Schmidt, Arvid Hage, Torsten Mans, François Légaré, and Hans Jakob Wörner. Highly stable, 54mj yb-innoslab laser platform at 0.5 kw average power. *Optics express*, 25(15):17549–17555, 2017.

[53] Luis E Zapata, Simon Schweisthal, Jelto Thesinga, Collette Zapata, Matthias Schust, Liu Yizhou, Mikhail Pergament, and Franz X Kaertner. Joule-class 500 hz cryogenic yb: Yag chirped pulse amplifier. In *CLEO: Science and Innovations*, pages SM4E–1. Optical Society of America, 2019.

[54] Clemens Herkommer, Peter Krötz, Robert Jung, Sandro Klingebiel, Christoph Wandt, Robert Bessing, Pierre Walch, Thomas Produit, Knut Michel, Dominik Bauer, et al. Ultrafast thin-disk multipass amplifier with 720 mj operating at kilohertz repetition rate for applications in atmospheric research. *Optics express*, 28(20):30164–30173, 2020.

[55] Yong Wang, Han Chi, Cory Baumgarten, Kristian Dehne, Alexander R Meadows, Aaron Davenport, Gabe Murray, Brendan A Reagan, Carmen S Menoni, and Jorge J Rocca. 1.1 j yb: Yag picosecond laser at 1 khz repetition rate. *Optics Letters*, 45(24):6615–6618, 2020.

[56] Adolf Giesen, H Hügel, A Voss, K Wittig, U Brauch, and H Opower. Scalable concept for diode-pumped high-power solid-state lasers. *Applied Physics B*, 58(5):365–372, 1994.

[57] U Brauch, Adolf Giesen, M Karszewski, Chr Stewen, and A Voss. Multiwatt diode-pumped yb: Yag thin disk laser continuously tunable between 1018 and 1053 nm. *Optics letters*, 20(7):713–715, 1995.

[58] Birgit Weichelt, Andreas Voss, Marwan Abdou Ahmed, and Thomas Graf. Enhanced performance of thin-disk lasers by pumping into the zero-phonon line. *Optics letters*, 37(15):3045–3047, 2012.

[59] Abdullah Alabbadi, Mikhail Larionov, and Florian Fink. High-power yb: Yag thin-disk laser with 80% efficiency pumped at the zero-phonon line. *Optics Letters*, 47(1):202–205, 2022.

[60] Robert Jung, Johannes Tümmler, and Ingo Will. Regenerative thin-disk amplifier for 300 mj pulse energy. *Optics express*, 24(2):883–887, 2016.

[61] Sandro Klingebiel, Marcel Schultze, Catherine Y Teisset, Robert Bessing, Matthias Häfner, Stephan Prinz, Martin Gorjan, Dirk Sutter, Knut Michel, Helena G Barros, et al. 220mj ultrafast thin-disk regenerative amplifier. In *CLEO: Science and Innovations*, pages STu4O–2. Optica Publishing Group, 2015.

[62] Brendan A Reagan, Mark Berrill, Keith A Wernsing, Cory Baumgarten, Mark Woolston, and Jorge J Rocca. High-average-power, 100-hz-repetition-rate, tabletop soft-x-ray lasers at sub-15-nm wavelengths. *Physical Review A*, 89(5):053820, 2014.

[63] Brendan A Reagan, Keith A Wernsing, Alden H Curtis, Federico J Furch, Bradley M Luther, Dinesh Patel, Carmen S Menoni, and Jorge J Rocca. Demonstration of a 100 hz repetition rate gain-saturated diode-pumped table-top soft x-ray laser. *Optics letters*, 37(17):3624–3626, 2012.

[64] Brendan A Reagan, Wei Li, Lukasz Urbanski, Keith A Wernsing, Chase Salsbury, Cory Baumgarten, Mario C Marconi, Carmen S Menoni, and Jorge J Rocca. Hour-long continuous operation of a tabletop soft x-ray laser at 50-100 hz repetition rate. *Optics express*, 21(23):28380–28386, 2013.

[65] M Schulz, R Riedel, A Willner, T Mans, C Schnitzler, P Russbueldt, J Dolkemeyer, E Seise, T Gottschall, S Hädrich, et al. Yb: Yag innoslab amplifier: efficient high repetition rate subpicosecond pumping system for optical parametric chirped pulse amplification. *Optics letters*, 36(13):2456–2458, 2011.

[66] Kyung-Han Hong, Chien-Jen Lai, Jonathas P Siqueira, Peter Krogen, Jeffrey Moses, Chun-Lin Chang, Gregory J Stein, Luis E Zapata, and Franz X Kärtner. Multi-mj, khz, 2.1 μm optical parametric chirped-pulse amplifier and high-flux soft x-ray high-harmonic generation. *Optics letters*, 39(11):3145–3148, 2014.

[67] Luis E Zapata, F Reichert, M Hemmer, and FX Kärtner. 250 w average power, 100 khz repetition rate cryogenic yb: Yag amplifier for opcpa pumping. *Optics letters*, 41(3):492–495, 2016.

[68] Paulius Mackonis and Aleksej M Rodin. Laser with 1.2 ps, 20 mj pulses at 100 hz based on cpa with a low doping level yb: Yag rods for seeding and pumping of opcpa. *Optics Express*, 28(2):1261–1268, 2020.

[69] Han Chi, Yong Wang, Aaron Davenport, Carmen S Menoni, and Jorge J Rocca. Demonstration of a kilowatt average power, 1 j, green laser. *Optics Letters*, 45(24):6803–6806, 2020.

[70] Vladimir Chvykov, Han Chi, Yong Wang, Kristian Dehne, Mark Berrill, and Jorge J Rocca. Demonstration of a side-pumped cross-seeded thin-slab pre-amplifier for high-power ti: Sa laser systems. *Optics Letters*, 47(14):3463–3466, 2022.

[71] Georg Korn, Andreas Thoss, Holger Stiel, Ullrich Vogt, Martin Richardson, Thomas Elsaesser, and Manfred Faubel. Ultrashort 1-khz laser plasma hard x-ray source. *Optics letters*, 27(10):866–868, 2002.

[72] Sébastien Corde, K Ta Phuoc, Guillaume Lambert, R Fitour, Victor Malka, Antoine Rousse, A Beck, and E Lefebvre. Femtosecond x rays from laser-plasma accelerators. *Reviews of Modern Physics*, 85(1):1, 2013.

[73] Reed Hollinger, Clayton Bargsten, Vyacheslav N Shlyaptsev, Vural Kaymak, Alexander Pukhov, Maria Gabriela Capeluto, Shoujun Wang, Alex Rockwood, Yong Wang, Amanda Townsend, et al. Efficient picosecond x-ray pulse generation from plasmas in the radiation dominated regime. *Optica*, 4(11):1344–1349, 2017.

[74] Fatholah Salehi, AJ Goers, GA Hine, Linus Feder, Donghoon Kuk, Bo Miao, Daniel Woodbury, Ki-Yong Kim, and HM Milchberg. Mev electron acceleration at 1 khz with< 10 mj laser pulses. *Optics letters*, 42(2):215–218, 2017.

[75] John T Morrison, Scott Feister, Kyle D Frische, Drake R Austin, Gregory K Ngirmang, Neil R Murphy, Chris Orban, Enam A Chowdhury, and WM Roquemore. Mev proton acceleration at khz repetition rate from ultra-intense laser liquid interaction. *New Journal of Physics*, 20(2):022001, 2018.

[76] AJ Gonsalves, K Nakamura, J Daniels, C Benedetti, C Pieronek, TCH De Raadt, S Steinke, JH Bin, SS Bulanov, J Van Tilborg, et al. Petawatt laser guiding and electron beam accel-

eration to 8 gev in a laser-heated capillary discharge waveguide. *Physical review letters*, 122(8):084801, 2019.

[77] Jean-Pierre Wolf. Short-pulse lasers for weather control. *Reports on Progress in Physics*, 81(2):026001, 2017.

[78] Thomas Produit, Pierre Walch, Clemens Herkommer, Amirhossein Mostajabi, Michel Moret, Ugo Andral, Antonio Sunjerga, Mohammad Azadifar, Yves-Bernard André, Benoît Mahieu, et al. The laser lightning rod project. *The European Physical Journal Applied Physics*, 93(1):10504, 2021.

[79] A Braun, G Korn, X Liu, D Du, J Squier, and G Mourou. Self-channeling of high-peak-power femtosecond laser pulses in air. *Optics letters*, 20(1):73–75, 1995.

[80] Arnaud Couairon and André Mysyrowicz. Femtosecond filamentation in transparent media. *Physics reports*, 441(2-4):47–189, 2007.

[81] L Bergé, S Skupin, R Nuter, Jérôme Kasparian, and Jean-Pierre Wolf. Ultrashort filaments of light in weakly ionized, optically transparent media. *Reports on progress in physics*, 70(10):1633, 2007.

[82] Sergey Mitryukovskiy. *Coherent secondary radiation from femtosecond laser filaments*. PhD thesis, École Polytechnique, 2014.

[83] John H Marburger. Self-focusing: theory. *Progress in quantum electronics*, 4:35–110, 1975.

[84] B La Fontaine, F Vidal, Z Jiang, CY Chien, Dl Comtois, A Desparois, TW Johnston, J-C Kieffer, H Pépin, and HP Mercure. Filamentation of ultrashort pulse laser beams resulting from their propagation over long distances in air. *Physics of plasmas*, 6(5):1615–1621, 1999.

[85] David W Koopman and KA Saum. Formation and guiding of high-velocity electrical streamers by laser-induced ionization. *Journal of Applied Physics*, 44(12):5328–5336, 1973.

[86] Megumu Miki, Yoshiro Aihara, and Takatoshi Shindo. Development of long gap discharges guided by a pulsed co2 laser. *Journal of physics D: Applied physics*, 26(8):1244, 1993.

[87] Megumu Miki, Takatoshi Shindo, and Yoshinori Aihara. Mechanisms of guiding ability of laser-produced plasmas on pulsed discharges. *Journal of physics D: Applied physics*, 29(7):1984, 1996.

[88] Andreas Schmitt-Sody, David French, William White, Adrian Lucero, William P Roach, and Victor Hasson. The importance of corona generation and leader formation during laser filament guided discharges in air. *Applied Physics Letters*, 106(12):124101, 2015.

[89] D Comtois, CY Chien, A Desparois, F Génin, G Jarry, TW Johnston, J-C Kieffer, B La Fontaine, F Martin, R Mawassi, et al. Triggering and guiding leader discharges using a plasma channel created by an ultrashort laser pulse. *Applied Physics Letters*, 76(7):819–821, 2000.

[90] DF Gordon, Antonio Ting, RF Hubbard, Eldridge Briscoe, C Manka, SP Slinker, AP Baronavski, HD Ladouceur, PW Grounds, and PG Girardi. Streamerless guided electric discharges triggered by femtosecond laser filaments. *Physics of Plasmas*, 10(11):4530–4538, 2003.

[91] Andreas Schmitt-Sody, Jennifer Elle, Adrian Lucero, Matthew Domonkos, Anthony Ting, and Victor Hasson. Dependence of single-shot pulse durations on near-infrared filamentation-guided breakdown in air. *AIP Advances*, 7(3):035018, 2017.

[92] Stellios Tzortzakis, Bernard Prade, Michel Franco, André Mysyrowicz, Stefan Hüller, and Patrick Mora. Femtosecond laser-guided electric discharge in air. *Physical Review E*, 64(5):057401, 2001.

[93] EW Rosenthal, I Larkin, A Goffin, Thomas Produit, Malte Christian Schroeder, J-P Wolf, and HM Milchberg. Dynamics of the femtosecond laser-triggered spark gap. *Optics Express*, 28(17):24599–24613, 2020.

[94] Thomas Produit, Pierre Walch, Guillaume Schimmel, Benoît Mahieu, Clemens Herkommer, Robert Jung, Thomas Metzger, Knut Michel, Yves-Bernard André, André Mysyrowicz, et al. Hv discharges triggered by dual-and triple-frequency laser filaments. *Optics express*, 27(8):11339–11347, 2019.

[95] Aurélien Houard, Vytautas Jukna, Guillaume Point, Yves-Bernard André, S Klingebiel, M Schultze, Knut Michel, Thomas Metzger, and André Mysyrowicz. Study of filamentation with a high power high repetition rate ps laser at 1.03 μm. *Optics express*, 24(7):7437–7448, 2016.

[96] Pierre Walch, Benoît Mahieu, Leonid Arantchouk, Y-B André, André Mysyrowicz, and Aurélien Houard. Cumulative air density depletion during high repetition rate filamentation of femtosecond laser pulses: Application to electric discharge triggering. *Applied Physics Letters*, 119(26):264101, 2021.

[97] Adam Higginson, Yong Wang, Han Chi, Andrew Goffin, Ilia Larkin, HM Milchberg, and JJ Rocca. Wake dynamics of air filaments generated by high-energy picosecond laser pulses at 1 khz repetition rate. *Optics Letters*, 46(21):5449–5452, 2021.

[98] Ursula Keller, Kurt J Weingarten, Franz X Kartner, Daniel Kopf, Bernd Braun, Isabella D Jung, Regula Fluck, Clemens Honninger, Nicolai Matuschek, and J Aus Der Au. Semiconductor saturable absorber mirrors (sesam's) for femtosecond to nanosecond pulse generation in solid-state lasers. *IEEE Journal of selected topics in QUANTUM ELECTRONICS*, 2(3):435–453, 1996.

[99] Rüdiger Paschotta and Ursula Keller. Ultrafast solid-state lasers. In *Ultrafast lasers*, pages 17–65. CRC Press, 2002.

[100] NV Kuleshov, AA Lagatsky, AV Podlipensky, VP Mikhailov, and G Huber. Pulsed laser operation of yb-doped ky (wo 4) 2 and kgd (wo 4) 2. *Optics letters*, 22(17):1317–1319, 1997.

[101] Peter Klopp, Valentin Petrov, Uwe Griebner, and Goetz Erbert. Passively mode-locked yb: Kyw laser pumped by a tapered diode laser. *Optics Express*, 10(2):108–113, 2002.

[102] RL Fork, OE Martinez, and JP Gordon. Negative dispersion using pairs of prisms. *Optics letters*, 9(5):150–152, 1984.

[103] J Körner, V Jambunathan, J Hein, R Seifert, M Loeser, M Siebold, U Schramm, P Sikocinski, A Lucianetti, T Mocek, et al. Spectroscopic characterization of yb3+-doped laser materials at cryogenic temperatures. *Applied Physics B*, 116(1):75–81, 2014.

[104] Han Chi, Kristian A Dehne, Cory M Baumgarten, Hanchen Wang, Liang Yin, Brendan A Reagan, and Jorge J Rocca. In situ 3-d temperature mapping of high average power cryogenic laser amplifiers. *Optics Express*, 26(5):5240–5252, 2018.

[105] Dmitrii Kouznetsov and Jean-François Bisson. Role of undoped cap in the scaling of thin-disk lasers. *JOSA B*, 25(3):338–345, 2008.

[106] Mu Wang, Guangzhi Zhu, Xiao Zhu, Yongqian Chen, Jing Dong, Hailin Wang, and Yefeng Qian. Thickness optimization for an anti-ase cap in a thin disk laser considering dioptric power and aberration-induced loss. *JOSA B*, 35(3):583–592, 2018.

[107] Dong Jun, Deng Peizhen, and Xu Jun. The growth of cr4+, yb3+: yttrium aluminum garnet (yag) crystal and its absorption spectra properties. *Journal of crystal growth*, 203(1-2):163–167, 1999.

[108] Jerome M Auerbach and Victor P Karpenko. Serrated-aperture apodizers for high-energy laser systems. *Applied optics*, 33(15):3179–3183, 1994.

[109] JR Vaill, DA Tidman, TD Wilkerson, and DW Koopman. Propagation of high-voltage streamers along laser-induced ionization trails. *Applied Physics Letters*, 17(1):20–22, 1970.

[110] KA Saum and David W Koopman. Discharges guided by laser-induced rarefaction channels. *The Physics of Fluids*, 15(11):2077–2079, 1972.

[111] JR Greig, DW Koopman, RF Fernsler, RE Pechacek, IM Vitkovitsky, and AW Ali. Electrical discharges guided by pulsed co 2-laser radiation. *Physical Review Letters*, 41(3):174, 1978.

[112] Takatoshi Shindo, Megumu Miki, Yoshinori Aihara, and Atsushi Wada. Laser-guided discharges in long gaps. *IEEE transactions on Power Delivery*, 8(4):2016–2022, 1993.

[113] Henri Pépin, D Comtois, F Vidal, CY Chien, A Desparois, TW Johnston, JC Kieffer, B La Fontaine, F Martin, FAM Rizk, et al. Triggering and guiding high-voltage large-scale leader discharges with sub-joule ultrashort laser pulses. *Physics of plasmas*, 8(5):2532–2539, 2001.

[114] Y-H Chen, S Varma, TM Antonsen, and HM Milchberg. Direct measurement of the electron density of extended femtosecond laser pulse-induced filaments. *Physical review letters*, 105(21):215005, 2010.

[115] Richard P Fischer, Antonio C Ting, Daniel F Gordon, Richard F Fernsler, Gregory P DiComo, and Phillip Sprangle. Conductivity measurements of femtosecond laser–plasma filaments. *IEEE transactions on plasma science*, 35(5):1430–1436, 2007.

[116] Guillaume Point, Carles Milián, Arnaud Couairon, André Mysyrowicz, and Aurélien Houard. Generation of long-lived underdense channels using femtosecond filamentation in air. *Journal of Physics B: Atomic, Molecular and Optical Physics*, 48(9):094009, 2015.

[117] Stellios Tzortzakis, Bernard Prade, Michel Franco, and André Mysyrowicz. Time-evolution of the plasma channel at the trail of a self-guided ir femtosecond laser pulse in air. *Optics communications*, 181(1-3):123–127, 2000.

[118] N Jhajj, EW Rosenthal, R Birnbaum, JK Wahlstrand, and HM Milchberg. Demonstration of long-lived high-power optical waveguides in air. *Physical Review X*, 4(1):011027, 2014.

[119] Friedrich Paschen. *Ueber die zum funkenübergang in luft: wasserstoff und kohlensäure bei verschiedenen drucken erforderliche potentialdifferenz...* JA Barth, 1889.

[120] Patrick Rambo, Jens Schwarz, and Jean-Claude Diels. High-voltage electrical discharges induced by an ultrashort-pulse uv laser system. *Journal of Optics A: Pure and applied optics*, 3(2):146, 2001.

[121] Miguel Rodríguez, Roland Sauerbrey, H Wille, Ludger Woeste, T Fujii, Y-B André, André Mysyrowicz, L Klingbeil, K Rethmeier, W Kalkner, et al. Triggering and guiding megavolt discharges by use of laser-induced ionized filaments. *Optics letters*, 27(9):772–774, 2002.

[122] Aurélien Houard, Ciro d'Amico, Yi Liu, Yves-Bernard André, Michel Franco, Bernard Prade, André Mysyrowicz, Estelle Salmon, Pascal Pierlot, and L-M Cleon. High current permanent discharges in air induced by femtosecond laser filamentation. *Applied physics letters*, 90(17):171501, 2007.

[123] K Sugiyama, T Fujii, M Miki, M Yamaguchi, A Zhidkov, E Hotta, and K Nemoto. Laser-filament-induced corona discharges and remote measurements of electric fields. *Optics letters*, 34(19):2964–2966, 2009.

[124] Benjamin Forestier, Aurélien Houard, Ivan Revel, Magali Durand, Yves-Bernard André, Bernard Prade, Amélie Jarnac, Jérôme Carbonnel, Marc Le Nevé, Jean-Claude De Miscault, et al. Triggering, guiding and deviation of long air spark discharges with femtosecond laser filament. *AIp Advances*, 2(1):012151, 2012.

[125] Kaimin Guo, Jingquan Lin, Zuoqiang Hao, Xun Gao, Zhenming Zhao, Changkai Sun, and Baozeng Li. Triggering and guiding high-voltage discharge in air by single and multiple femtosecond filaments. *Optics Letters*, 37(2):259–261, 2012.

[126] Y-H Cheng, JK Wahlstrand, N Jhajj, and HM Milchberg. The effect of long timescale gas dynamics on femtosecond filamentation. *Optics express*, 21(4):4740–4751, 2013.

[127] JK Wahlstrand, N Jhajj, EW Rosenthal, S Zahedpour, and HM Milchberg. Direct imaging of the acoustic waves generated by femtosecond filaments in air. *Optics Letters*, 39(5):1290–1293, 2014.

[128] Aurélien Houard, Pierre Walch, Thomas Produit, Victor Moreno, Benoit Mahieu, Antonio Sunjerga, Clemens Herkommer, Amirhossein Mostajabi, Ugo Andral, Yves-Bernard André, et al. Laser-guided lightning. *Nature Photonics*, 2023.

[129] Brendan A Reagan, Alden H Curtis, Keith A Wernsing, Federico J Furch, Bradley M Luther, and Jorge J Rocca. Development of high energy diode-pumped thick-disk yb: Yag chirped-pulse-amplification lasers. *IEEE Journal of Quantum Electronics*, 48(6):827–835, 2012.

[130] Andreas Schmitt-Sody, Heiko G Kurz, Luc Bergé, Stefan Skupin, and Pavel Polynkin. Picosecond laser filamentation in air. *New Journal of Physics*, 18(9):093005, 2016.

[131] John Christoher Martin. Nanosecond pulse techniques. *Proceedings of the IEEE*, 80(6):934–945, 1992.

[132] Richard J Adler. Pulse power formulary. Technical report, North Star Research Corp. Albuquerque NM, 1989.

[133] WA Gambling and H Edels. The high-pressure glow discharge in air. *British Journal of Applied Physics*, 5(1):36, 1954.

[134] Robert H Stark and Karl H Schoenbach. Direct current glow discharges in atmospheric air. *Applied Physics Letters*, 74(25):3770–3772, 1999.

[135] Sander Nijdam, Jannis Teunissen, and Ute Ebert. The physics of streamer discharge phenomena. *Plasma Sources Science and Technology*, 29(10):103001, 2020.

[136] Bruno La Fontaine, Daniel Comtois, Ching-Yuan Chien, Alain Desparois, Frederic Genin, Genevieve Jarry, Tudor Johnston, Jean-Claude Kieffer, Francois Martin, Raafat Mawassi, et al. Guiding large-scale spark discharges with ultrashort pulse laser filaments. *Journal of Applied Physics*, 88(2):610–615, 2000.